Anisotropic, rate-dependent ductile fracture of Ti-6Al-4V alloy

Miguel Ruiz de Sotto, Véronique Doquet, Patrice Longère, Jessica Papasidero

Anisotropic, rate -dependent ductile fracture of Ti-6Al-4V alloy

Miguel Ruiz de Sotto[1], Véronique Doquet[2,]*, Patrice Longère[3], Jessica Papasidero[1]

[1]*Safran Aircraft Engines, Rond-point René Ravaud, 775500 Réau, France*

[2]*Laboratoire de Mécanique des Solides, CNRS UMR 7649, Ecole Polytechnique, Institut Polytechnique de Paris, 91128 Palaiseau, France*

[3]*ICA, Université de Toulouse, ISAE-SUPAERO, MINES ALBI, UPS, INSA, CNRS, 31000, Toulouse, France.*

*Corresponding author
Email address: doquet@lms.polytechnique.fr

Abstract

An extensive experimental campaign was run to investigate the influence of the loading direction, stress state (triaxiality ratio ranging from -0.5 to 1), and strain rate (from 10^{-3} to $1.5x10^{3}s^{-1}$) on the ductile fracture of Ti-6Al-4V titanium alloy. Microscopic and macroscopic observations provided some insight into the shear-driven or micro-voiding-controlled damage mechanisms prevailing at low and high triaxiality ratios, respectively. Numerical simulations were run to determine the local loading paths to fracture in terms of plastic strain as a function of stress triaxiality ratio and Lode parameter. The ductility was found to be anisotropic, but only weakly dependent on the strain rate in the considered range. The anisotropy in ductility was different in tension (maximum along DD) and in compression (maximum along ND). The fracture strain decreased with the absolute value of the triaxiality, with a maximum close to zero. No clear correlation with the Lode parameter was found.

Keywords: Ductile fracture, titanium alloy, triaxiality; Lode parameter , anisotropy; temperature, strain rate

1 Introduction

To be certified some critical parts of aeronautical and space structures need to be designed against accidental overloads to prevent their fracture. This is the case for aircraft engines fan blades that should be able to withstand ballistic events, like bird strike or fan blade loss. During such events the fan blades leading edge – often made of Ti-6Al-4V titanium alloy – undergoes large deformation, high strain rate, non-proportional multiaxial loading and load reversals. The risk of ductile fracture must accordingly be assessed for these complex and widely variable conditions to be further accounted for in the design process. The first stage towards such an assessment was to formulate, calibrate and implement into a commercial finite element computation code (LS-DYNA) a proper constitutive model for Ti-6Al-4V titanium alloy. This stage, detailed in a companion paper, see Ruiz de Sotto et al. (2020), is only briefly recalled here in Appendix since the present paper focuses on damage and fracture.

Experimental works available in the literature, see e.g. Hooputra et al. (2004), Barsoum and Faleskog (2007), Haltom et al. (2013), have evidenced two regimes of ductile fracture of metals and alloys: a high hydrostatic tension regime, in which fracture results from micro-void nucleation, growth and coalescence, and a shear-pressure-dominated regime, in which fracture is controlled by shear strain localization, and decohesion. This loading-dependent competition between void growth-induced fracture and shear decohesion-induced fracture can be modelled

by more or less explicitly accounting for the stress triaxiality ratio χ, expected to control micro-void collapse/growth, and the shear stress ratio η, expected to control micro-void flattening and subsequent shear decohesion, or the Lode angle θ or parameter $L=-\cos(3\theta)$, which additionally allows a differentiation of loading types involving similar shear stress states. Starting from the definition of the pressure and maximum shear stress $p=-\mathrm{Tr}\,\underline{\underline{\sigma}}/3=-(\sigma_1+\sigma_2+\sigma_3)/3$, and $\tau_{\max}=(\sigma_1-\sigma_3)/2$ with respect to the ranked principal stresses $\sigma_p=\mathrm{eig}_p\left(\underline{\underline{\sigma}}\right)\ (\sigma_1\geq\sigma_2\geq\sigma_3)$, one can express the stress triaxiality and shear stress ratios $\chi=-p/q$ and $\eta=\tau_{\max}/q$, where the equivalent stress q can merely correspond to Von Mises stress σ_M, i.e. $q=\sigma_M$, or can take a more complex form when e.g. plastic anisotropy is involved – as it is the case in the present work. The Lode parameter L which is defined as $L=\left[2\sigma_2-(\sigma_1+\sigma_3)\right]/(\sigma_1-\sigma_3)$ can accordingly be rewritten as $L=(3/2)\left(\left[2\sigma_2/(\sigma_1-\sigma_3)\right]-(\chi/\eta)\right)$.

Ductile fracture criteria may be derived from continuum damage mechanics (CDM)-based constitutive models (involving the micro-void volume fraction f, or more generally a damage internal variable D), or directly written in terms of critical strain at fracture ε_F^p or stress at fracture σ_F.

For example, Johnson and Cook (1985) investigated the fracture of copper and steels and proposed a failure criterion describing a monotonic dependence of ε_F^p on χ in the [0;1.2] χ-range (as well as on strain rate and temperature). Bao and Wierzbicki (2004) evidenced a non-monotonic dependence of ε_F^p on χ in the [-1/3;1] χ-range for AA2024-T351 aluminum alloy, and accordingly Bao and Wierzbicki (2005) proposed a 2-regime based dependence of ε_F^p on χ. In the same time, Wierzbicki and Bao (2005) reported a criterion accounting explicitly for χ and L in the expression of ε_F^p. For the same aluminum alloy for which they obtain different fracture conditions in the [0;1] χ-range, i.e. a monotonic decrease of ductility, Papasidero et al. (2015) identified a θ- and loading direction-dependent σ_F (and further ε_F^p for a given strain hardening law) derived from a Mohr-Coulomb like fracture initiation surface. Based on tests carried out on AA7108-T6 aluminum alloy in the [0;2] χ-range, Hooputra et al. (2004) developed two competing ε_F^p related fracture criteria, involving χ and η, respectively. Fracture was assumed to occur as soon as one of the two criteria is met. They also documented the influence of the loading direction and strain rate. In this context of anisotropic materials, Ha et al. (2019) and Korkolis et al. (2010) underlined the importance of using an appropriate anisotropic plasticity model, in order to get correct predictions of ductile failure.

A number of studies dedicated to the ductile fracture of Ti-6Al-4V titanium alloy can also be found in the literature.

For example, Giglio et al(2012), and Allahverdizadeh et al. (2015) investigated the quasi-static fracture of bimodal Ti-6Al-4V for nil and positive χ ranging from 0 to 1, based on combined tension or compression plus torsion tests on smooth or notched cylinders, as well as tensile tests on various types of flat samples. They attempted to describe the fracture locus using either Bao-Wierzbicki's model (2004), or a coupled plasticity-damage model. The errors on the predicted fracture displacement or rotation in both cases were often 20-50%, probably due to the use of a too basic constitutive model, i.e. not accounting for anisotropy. Later, Zhang et al. (2020)used the previous set of experimental data to identify a coupled plasticity-damage model, accounting for anisotropy, tension-compression asymmetry, as well as combined isotropic and kinematic hardening. The agreement between model predictions and experimental data for fracture was significantly improved. The same authors had developed an anisotropic thermo-elasto-viscoplastic model coupled with isotropic ductile damage , Zhang et al. (2018), but their application to Ti-6Al-4V was limited to yield surface predictions at various temperatures. Vilotic et al (2016) performed confined ring upsetting tests on Ti-6Al-4V. They observed that ductile fracture occurs even at χ as low as -0.63, and reported a monotonic decrease of ductility as triaxiality rises from -0.63 to +0.43. Tancogne-Dejean et al (2016) investigated the quasi-static ductile fracture of additively-manufactured Ti-6Al-4V using various types of flat notched samples cut along various directions. They used a non-associated anisotropic Hill48 flow rule, which approximately fitted the load-displacement curves, and proposed a probabilistic Mohr-Coulomb like fracture initiation criterion and further σ_F leading to a χ - and L -dependence of ε_F^p . The experimental scatter in ε_F^p was mainly attributed to the microstructural heterogeneity of the material (presence of "macro-zones" with correlated grains orientations inside, inherited from former beta grains). Wang et al. (2019) documented the anisotropic and temperature-dependent ductile fracture of Ti-6Al-4V thin sheets between room temperature (RT) and 800°C, through tensile tests on smooth and notched samples, as well as shear tests, along various loading directions, plus Nakajima tests, at strain rates between 0.01 and $1s^{-1}$. They reported a nearly constant ductility up to 400°C, and a substantial rise beyond. The anisotropy of ε_F^p was quite significant for shear loading (with nearly a factor of two between the most and least ductile directions), but much less at χ above 1/3 (less than 15% difference). They used the Barlat-Lian1989 anisotropic yield criterion with an associated flow rule, and an incremental damage accumulation model, plus a localization criterion to determine the fracture conditions, with some success, but also some discrepancies. Chen et al. (2018) investigated the ductile fracture of bimodal Ti-6Al-4V in compression between $2.5x10^3$ and 10^5 s^{-1} at room temperature or at 100°C. They reported that ε_F^p increases with the strain rate, and is higher at 100°C than at room temperature. They proposed a coupled plasticity-damage model, but they did not investigate anisotropy effects nor the quasi-static regime. Huang et al. (2018) studied the effect of χ and strain rate on the ductile fracture of bimodal Ti-6Al-4V at room temperature, 150°C, and 300°C through quasi-static and dynamic tensile tests on smooth or notched cylindrical specimens, and reported a monotonic decrease of ε_F^p as χ rose from 0.45 to 1.05. Ductility increased with the temperature, and was higher at high strain rates than in the quasi-static regime. They used Johnson-Cook plasticity and damage models, see Johnson and Cook (1985), to reproduce the

data. They however did not investigate anisotropy effects. Gross and Ravi-Chandar (2016) performed simulations of tension and shear tests run in the framework of the 2014 Sandia Fracture Challenge at two different strain rates in various loading directions, using Hill48 flow rule, the Johnson-Cook model (1985) to capture strain rate and temperature effects, plus a ε_F^p, assumed to decrease monotonically with χ in the range -0.63 to 3, and independent of the loading direction. The agreement with experimental data was incomplete, which was attributed to an imperfect modelling of plastic flow. Pack and Roth (2016) analysed the same test series, using the Hill'48 anisotropic yield function and the Johnson–Cook strain rate hardening and temperature softening functions, as well, but fitted a strain rate dependent Mohr–Coulomb like fracture initiation criterion. They conclude that L cannot be neglected.

From this brief literature survey, it appears that ductile fracture of Ti-6Al-4V alloy is generally reproduced by decoupled approaches of viscoplasticity and damage rarely correlated with microscopic observations, and that in spite of a substantial number of studies, a complete picture of the combined effects of the loading direction, strain rate, stress state on ductile damage and fracture is still missing for Ti-6Al-4V titanium alloy. Since all these aspects are crucial for the design of impact-resistant aircraft engine fan blades, an extensive experimental study was run in the present work in a wide range of χ, strain rate, and loading directions, as representative of possible accidental conditions for aircraft fan blades as possible.

Within an engineering-oriented approach, two questions had to be addressed. Is there any need for a coupled damage-plasticity model, or is a ε_F^p-based fracture criterion sufficient? And in the latter case, is it possible to express the fracture criterion as a function of the stress triaxiality ratio χ or/and Lode parameter L, as usually done?

In an attempt to answer these questions, a large series of tests, either leading to fracture, or interrupted just before fracture were carried out, and followed by the microscopic observation of the damage mechanisms. In parallel, numerical analyses were conducted aiming at investigating the influence of the loading direction, stress state (χ ranging from -0.5 to 1), and strain rate (from 10^{-3} to $1.5\text{x}10^{3}\text{s}^{-1}$) on the ductility of Ti-6Al-4V titanium alloy.

The paper is organised as follows. In Section 2 the experimental procedure, including the material mechanical response in terms of stress-strain and load-displacement curves, is briefly presented. The damage and fracture mechanisms are then described in details in Section 3. Section 4 gathers the numerical simulations of some representative loading cases for the extraction of local values unreachable by the experiments. In Section 5 the experimental and numerical results are combined to identify the fracture locus of the material. Concluding remarks are finally gathered in Section 6.

2 Experimental investigation

2.1 Material under consideration and geometry of the specimens

The Ti-6Al-4V titanium alloy under consideration was provided in the form of a 16 mm-thick

cold-rolled sheet. Its microstructure is bimodal (see Figure 1), and the size of the equiaxed primary α phase nodules ranges from a few microns up to 30 μm. Secondary α laths, 5 to 20μm long and a few μm wide are visible within the partially transformed β phase (dissolved by the chemical attack) on the atomic force microscopy (AFM) image (Figure 1d). The spatial distribution of the α and β phases does not seem completely random, since in many places, rows of α nodules parallel to the rolling direction (RD) or (in-plane) transverse direction (TD), and perpendicular to (through-thickness) normal direction (ND) can be observed, in-between elongated areas of partially transformed β phase (Figure 1a and b). Electron backscattering diffraction (EBSD) mappings of grains orientations (not reproduced here, see Figure1 in [1]) reveal the existence of hundreds of μm wide ``macro-zones" with a different orientation, inherited from the orientation of the former β grains. However, even though the texture is locally pronounced, the global texture measured by X-ray diffraction is actually moderate (the maximum density of poles is at most 4.4 times that for a random texture), with the c axes of HCP crystals mostly normal to ND, and clustered along RD or TD.

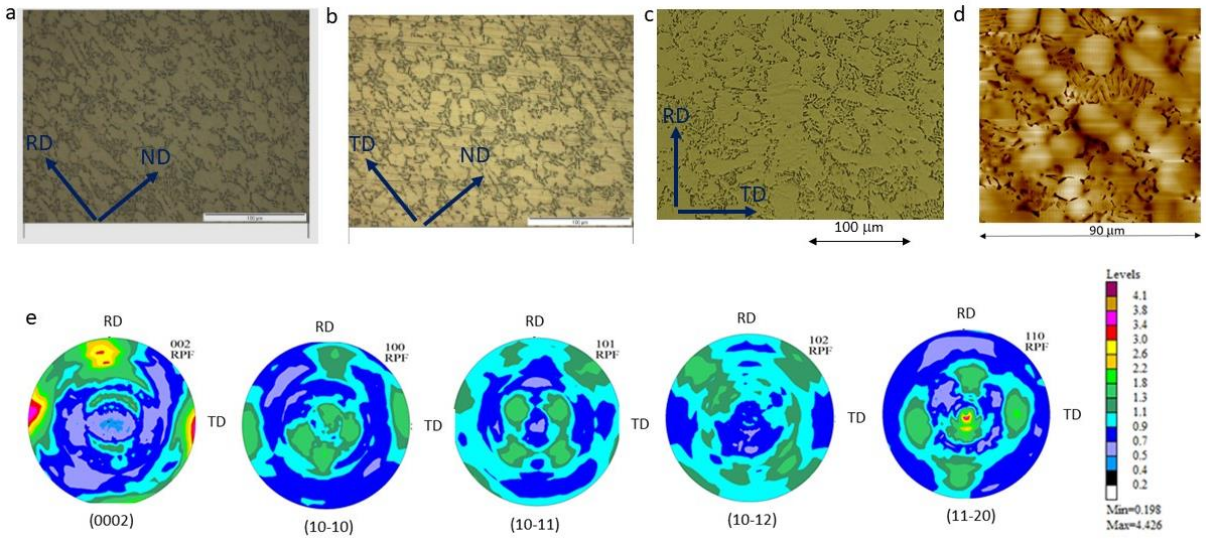

Figure 1: a-c) Optical images of the microstructure a) in the RD-ND plane, b) in the TD-ND plane, c) in the RD-TD plane, d) AFM image in the RD-TD plane, and e) pole figures for the α phase obtained by X-ray diffraction

Various types of specimens have been machined along four directions: the RD, TD and ND, as well as a (in-plane) diagonal direction (DD) in the RD-TD plane, at 45° with respect to the rolling direction. The specimens have been designed in order to investigate a wide range of χ and L, viz.$\chi \in [-1,1.2]$ and $L \in [-1,1]$. As a reminder, Table 1 reports the values of χ, η and L for a few loading cases.

Table 1: A few loading types and their corresponding values of stress triaxiality ratio χ, shear stress ratio η, and Lode parameter, L.

	σ_1	σ_2	σ_3	p	τ_{max}	$q=\sigma_M$	χ	η	χ/η	L
Equi-biaxial compression	0	$-\sigma$	$-\sigma$	$2\sigma/3$	$\sigma/2$	σ	$-2/3$	$1/2$	$-4/3$	-1
Compression	0	0	$-\sigma$	$\sigma/3$	$\sigma/2$	σ	$-1/3$	$1/2$	$-2/3$	1
Shear	τ	0	$-\tau$	0	τ	$\sqrt{3}\tau$	0	$1/\sqrt{3}$	0	0
Tension	σ	0	0	$-\sigma/3$	$\sigma/2$	σ	$1/3$	$1/2$	$2/3$	-1
Equi-biaxial tension	σ	σ	0	$-2\sigma/3$	$\sigma/2$	σ	$2/3$	$1/2$	$4/3$	1

Figure 2 shows the geometries of the specimens leading to nil and positive χ, with the tension-induced shear specimen inspired from the work of Roth and Mohr(2018), and Figure 3 those leading to negative χ inspired from Couque (2003) and Meyers et al (2001). Shorter smooth tensile specimens were used for the normal direction, along which the length is limited by the plate thickness. The cross section remained the same, but the gauge length was reduced to 4mm. The average values of χ indicated in these figures were obtained from preliminary finite element simulations using the constitutive model detailed in Ruiz de Sotto et al (2020-a) and outlined in Appendix. The thickness of the flat specimens is not very large compared to the size of the "macro-zones", but it is comparable to the thickness of the leading edge of the fan blades.

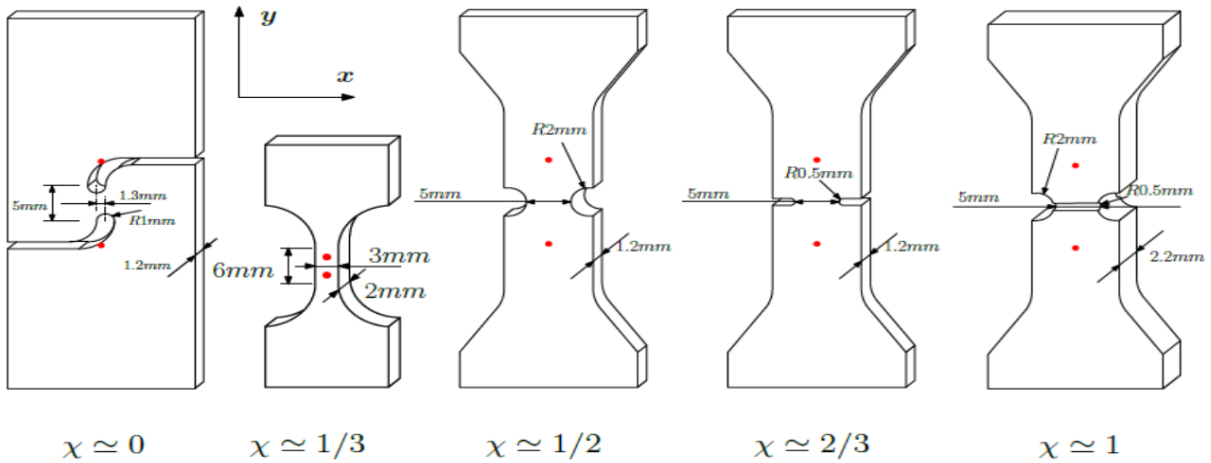

Figure 2: Flat specimen geometries used to cover the triaxiality range [0,1]. The red dots indicate the gage length of the extensometer.

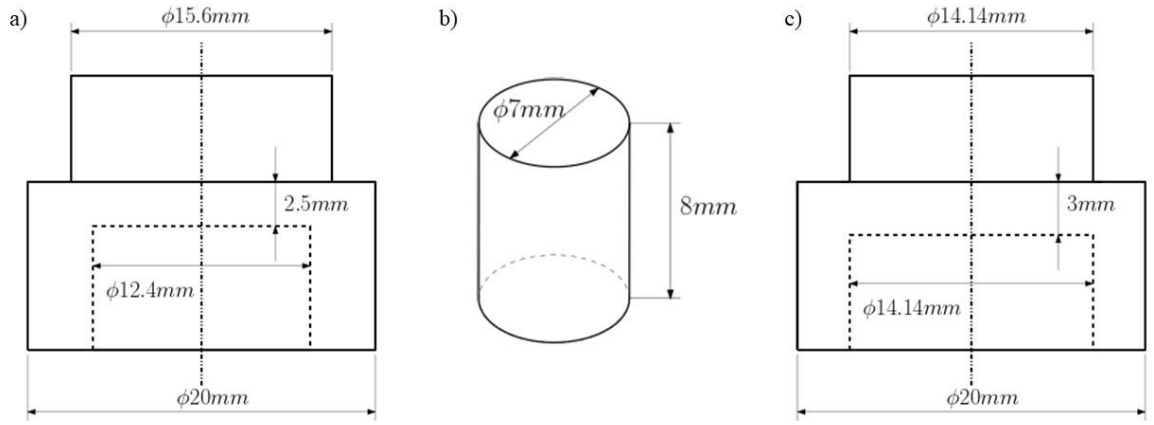

$\chi \simeq -1/2$ $\chi \simeq -1/3$ $\chi \simeq -1/5$

Figure 3: Axisymmetric specimen geometries used to cover the stress triaxiality range $\chi \in [-1/2,\ 0]$. Hat-shaped specimens have been designed following Couque (2003) and Meyers et al. (2001)

Tension, compression and shear tests were carried out at room temperature and at low strain rate (typically ranging between $|\dot{\varepsilon}| \simeq 10^{-4}s^{-1}$ and $|\dot{\varepsilon}| \simeq 10^{-1}s^{-1}$) using standard tension-compression testing machines, and at high strain rate (typically of the order of $|\dot{\varepsilon}| \simeq 1.5x10^{3}s^{-1}$) using split Hopkinson pressure bar (SHPB) set-ups. In order to assess repeatability, two to four test repetitions were carried out for most tests. In the case of compression tests, a clip-on extensometer was mounted on the rigid plates compressing the sample, and grease was applied as lubricant on the top and bottom sides in order to minimize the barreling effect. For dynamic tension tests, the load-inversion device developed by Dunand et al. (2013) and modified by Roth et al. (2015) was used. In these tests, the strain field in the sample was obtained by digital image correlation (DIC) using Vic-2D software, based on images captured by a Phantom v7.3 high speed camera. A frame rate of 10^5 Hz with a resolution of 304x64 pixel^2 was employed to monitor a 10x3mm^2 area covered with speckle painting. The global strain in the gage length was measured using a virtual extensometer based on the distance between two dots on the specimen, see Figures 2-3. Table 2 summarizes the test conditions.

Table 2: Loading conditions

Specimen type	Loading direction	Strain or displacement rate
Shear	RD, TD, DD	$1.6x10^{-3}$ mm/s
Smooth tension	RD, TD, DD ND	10^{-3} s^{-1}, 10^{-2} s^{-1}, $3x10^{2}$ s^{-1}, 10^{3} s^{-1}, $1.5x10^{3}$ s^{-1} 10^{-3} s^{-1}, 10^{-2} s^{-1}
Simply notched 2mm	RD, TD, DD	$1.6x10^{-3}$ mm/s
Simply notched 0.5mm	RD, TD, DD	$1.6x10^{-3}$ mm/s
Doubly notched 0.5mm	RD, TD, DD	$1.6x10^{-3}$ mm/s
Smooth compression	RD, TD, DD, ND	10^{-3} s^{-1}, 10^{-2} s^{-1}, $3x10^{2}$ s^{-1}, 10^{3} s^{-1}
Meyer compression	RD, TD, ND	10^{-3} s^{-1}, 10^{3} s^{-1}

Couque compression	RD, TD, ND	10^{-3} s^{-1}, 10^{3} s^{-1}

2.2 Mechanical characterization

In this section, the stress-strain and load-displacement curves obtained under tension, compression and shear loading on smooth and notched specimens at various strain rates are reported. For confidentiality reason, stress and load values are normalised with respect to the yield stress (or load) along RD at room temperature, at a strain rate of $10^{-3}s^{-1}$. For notched and shear specimens, the term "apparent strain" refers to the relative displacement measured by the virtual extensometer divided by its gage length (distance between the two reference dots).

First, the influence of the loading direction and strain rate on the flow curves under uniaxial compression or tension is depicted in Figures 4 and 5. The end point of each curve corresponds to fracture. The curves obtained by simulation using the constitutive model outlined in Appendix are superimposed in Figure 4. According to Figure 4, the material exhibits strain hardening, and a higher yield stress along TD (along which most of the c axes, - known as a "hard direction" of the α phase- cluster), followed by RD (along which c axes also cluster, but to a lesser extent), DD and finally a lower yield stress along ND (normal to most c axes). It also shows a significant tension-compression asymmetry.
According to Figure 5, the material also exhibits strain rate hardening, as expected for a titanium alloy. This strain rate dependence for RD was also observed for the other loading directions.
All these specificities, as well as a pronounced kinematic hardening (not documented here) were captured by the constitutive model detailed in Ruiz de Sotto et al. (2020-a) and more briefly recalled in Appendix.

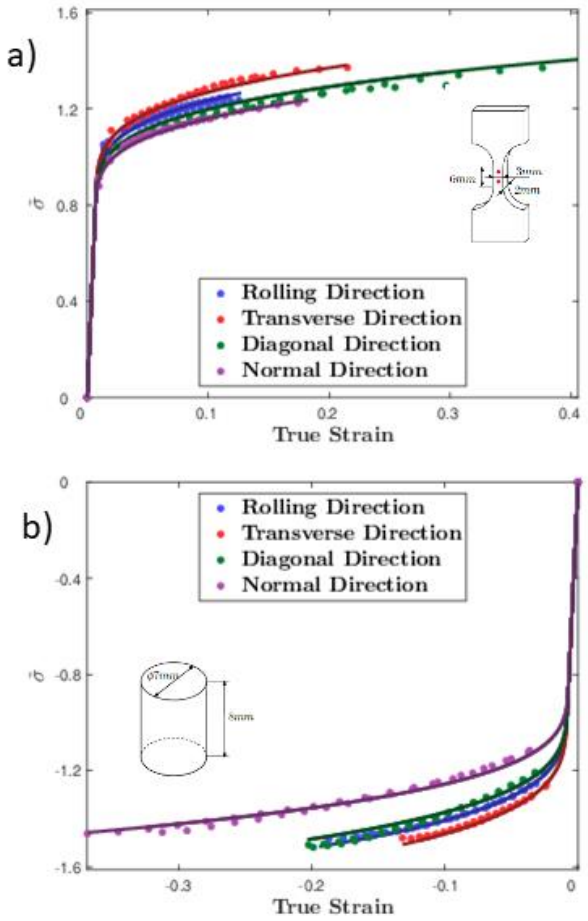

Figure 4: Normalized stress-strain curves along various loading directions at $10^{-3}s^{-1}$ in a) tension and b) compression. The solid line corresponds to simulations using the constitutive model described in Appendix

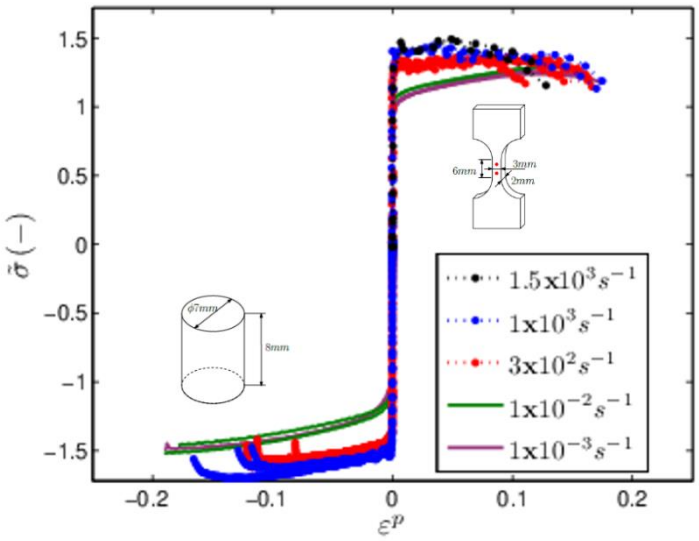

Figure 5: Normalized stress-strain curves for tension and compression along RD at various strain rates

The macroscopic fracture strain and final necking-induced variations in width w, thickness t,

and cross-section area A, of the smooth specimens broken under tension along RD, TD, ND or DD at different loading rates are reported in Table 3. They are expressed as

$$\begin{cases} \eta_w = \dfrac{w_f - w_o}{w_o} \\ \eta_t = \dfrac{t_f - t_o}{t_o} \\ \eta_A = \dfrac{A_f - A_o}{A_o} \end{cases} \qquad \textbf{Eq. 1}$$

where the subscripts o and f stand for initial and final (at fracture). The variation of the axial fracture strain with the loading direction and strain rate is also plotted in Figure 6, without any averaging of duplicate test results.

Table 3: Fracture strain and necking of smooth tensile specimens. The nominal dimensions were used as a reference for the quasi-static tests. Since the tests have been repeated, the values are averages over the number of broken samples.

Strain Rate		$T = 25^oC$		
		$10^{-3}s^{-1}$	$350s^{-1}$	$1500\ s^{-1}$
Fracture Strain ε_N^F	RD	16.9%	16.2%	13.4%
	DD	44.2%	20.7%	14.1%
	TD	21.2%	15.0%	18.8%
	ND	16.7%		
Width $\eta_w = \dfrac{\omega_f - \omega_o}{\omega_o}$	RD	16.1%	11.0%	12.4%
	DD	20.7%	17.0%	18.4%
	TD	16.1%	8.6%	19.0%
Thickness $\eta_t = \dfrac{t_f - t_o}{t_o}$	RD	23.1%	17.1%	26.6%
	DD	29.7%	18.5%	19.9%
	TD	24.5%	18.8%	33.8%
Cross-section $\eta_A = \dfrac{A_f - A_o}{A_o}$	RD	35.4%	26.2%	35.8%
	DD	44.3%	32.4%	34.6%
	TD	36.7%	25.8%	46.3%

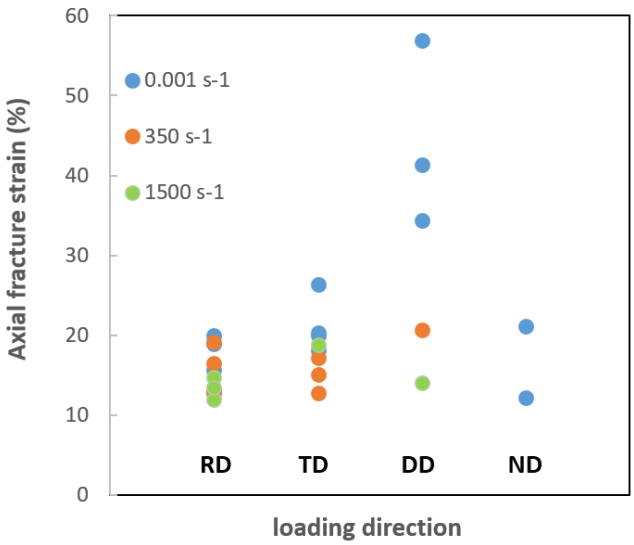

Figure 6: Variation of the axial tensile fracture strain with the loading direction and strain rate

The scatter from one sample to the other for the same loading conditions, as well as the different observed trends, depending on the criterion used to assess ductility (axial fracture strain, reduction in width, thickness or cross section) make the analysis of the anisotropy in terms of resistance to fracture of the material somewhat tricky. The scatter in experimental data is attributed to the presence of the aforementioned "macro-zones", as the dimensions of these zones approaches the thickness of the tested specimens, which is itself comparable to that of the leading edge of the fan blades.

The only clear characteristics is a nearly twice higher ductility along DD than along any other direction. This might be because DD is more favourable to prismatic glide than RD and TD (along which (10-10) directions tend to cluster) and has the possibility to activate basal slip to accommodate the plastic strain, contrary to all three other directions (since the c axes are mostly along RD and TD, see Figure 1e). Wang et al. (2019) also underlined the highest ductility of a thin Ti-6Al-4V sheet along DD.

Available data do not evidence any significant difference in tensile ductility between RD and TD, which is consistent with the quasi symmetry of the pole figures (Figure 1e), and the absence of a morphological difference of the microstructure between those two directions.

The limited amount of tensile data along ND (due to the impossibility, with the available experimental set-up, to perform high strain rate tests on such small specimens) does not allow any conclusion. The thickness reduction for specimens pulled along RD, TD and DD is more pronounced than their width reduction, which is consistent with the easiest plastic flow along ND (see Figure 4).

Contrary to what is observed on those smooth tensile specimens, for which the ductility along ND does not seem very different than along RD and TD, smooth cylindrical specimens compressed along ND failed at a much higher strain (38%) than along RD (25%), TD (16%) or even DD (28%). This is consistent with the results of Coghe et al. (2012) who also reported a higher compressive ductility of Ti-6Al-4V along a direction normal to most c axes, due to the

activation of {10-12} <-1011> “tensile twins” (a misleading term which means that these twins induce an extension along the c axis). Therefore, Ti-6Al-4V not only exhibits an anisotropic ductility, but this anisotropy is different in tension (maximum ductility along DD) and in compression (maximum ductility along ND).

Regarding the effect of the loading rate, no simple rule can be drawn either, since based on the reduction in width and thickness, ductility seems to drop at $\dot{\varepsilon} \simeq 350s^{-1}$ but to rise again at $\dot{\varepsilon} \simeq 1500s^{-1}$, sometimes reaching higher values than in the quasi static regime. This rise cannot be attributed to an enhancement of ductility by self-heating, since the temperature has been estimated to rise by at most 140°C at $1.5x10^{3}s^{-1}$ Ruiz de Sotto (2020-b), and additional tensile tests run at 170°C yielded approximately the same ductility as at room temperature. The rise might perhaps be due to micro-inertia effects that delay microvoids coalescence, as suggested by Jacques et al.(2012) . It might also result from an increasing accommodation of plastic strain by mechanical twinning, shown by Coghe et al. (2012) to become twice more active at 10^{3} s^{-1} than at $10^{-3}s^{-1}$ in Ti-6Al-4V. Note that Huang et al. (2018) reported a higher ductility for Ti-6Al-4V at $10^{3}s^{-1}$ than at $10^{-3}s^{-1}$.
By order of importance of its effect on ductility, it seems that the loading direction with respect to the cold-rolled sheet (thickness as opposed to width) comes first, then the in-plane loading direction (RD, DD, TD), followed by the loading rate, for which no rule can be drawn.

Figure 7 shows the normalized force vs. apparent strain for the flat, notched tension specimens pulled along TD until fracture. As expected, the resistance and apparent strain at fracture are highly dependent on the notch radii, and resulting χ. The highest force and lowest nominal strain at fracture are observed for the doubly notched specimen ($\chi \simeq 1$), while both simply notched specimens ($\chi \simeq 1/2, 2/3$) exhibit the same peak load, but a lower fracture strain for the smallest notch radius. Similar effects were observed for the other loading directions.

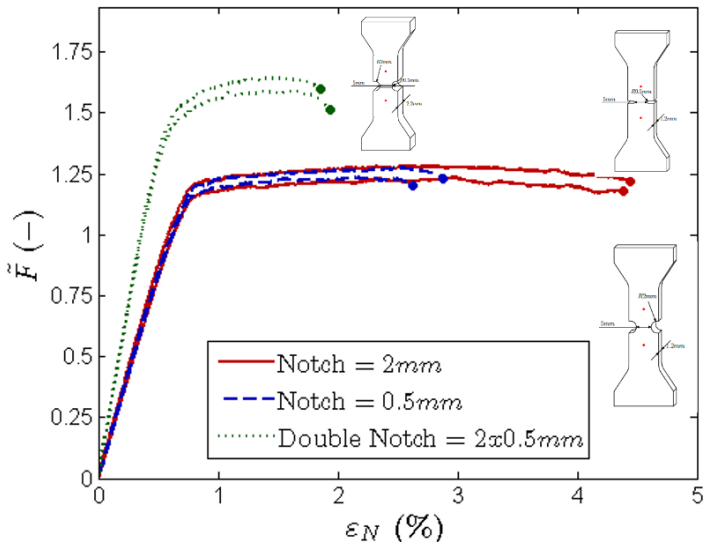

Figure 7: Normalized load versus apparent strain for tensile tests along TD on notched specimens. Displacement rate: 1.6 $x10^{-3}mms^{-1}$. Fracture is denoted by a circle

Figure 8 shows the load-apparent strain curves for two tension-induced shear specimens pulled until fracture along TD. Strain hardening, associated with a large strain at fracture can be noticed (and the same observation was made in the other loading directions).

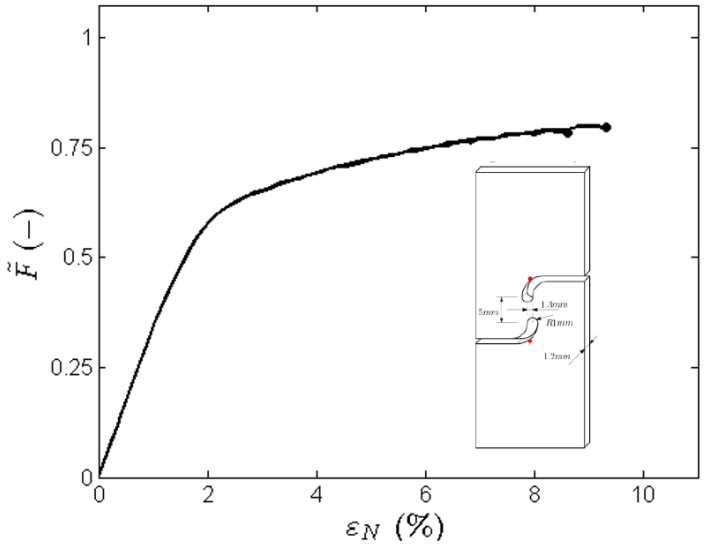

Figure 8: Normalized load versus apparent strain for shear specimens pulled along TD. Displacement rate: $1.6\text{x}10^{-3}\text{mms}^{-1}$. Fracture is denoted by a circle

Finally, Figure 9 shows the normalized force vs. apparent strain curves for Couque ($\chi \simeq -1/2$) and Meyers ($\chi \simeq -1/5$) type hat-shaped specimens. For each geometry, one test was carried out until fracture and the other test was interrupted for further microscopic observations. As expected, the combined effects of shear and compression on Couque's sample produce a higher load (higher pressure), as compared to Meyers's geometry (lower pressure). As the two geometries involve very different stress and strain states, the corresponding apparent axial strain values cannot be directly compared.

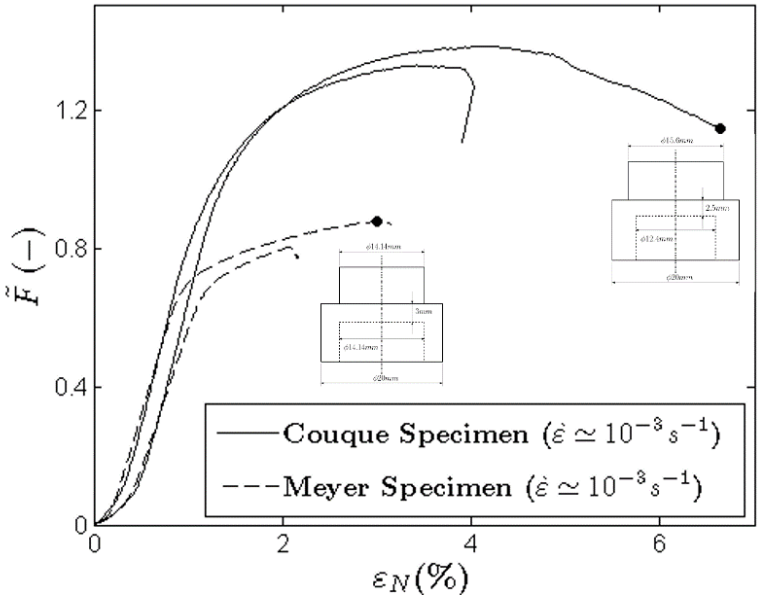

Figure 9: Normalized load versus apparent strain for hat-shaped specimens compressed along

ND. Displacement rate: $8x10^{-3}mms^{-1}$. Fracture is denoted by a circle

2.3 Damage and fracture characterization

Observations of fractured samples, as well as observations after interrupted tests, were carried out using scanning electron microscopy (SEM). For that purpose, mechanical polishing with sandpaper, followed by electro-polishing (using Struers A3 solution and a tension of 20V) or ion polishing was thus performed on longitudinal sections of the samples. The results are reported with respect to χ.

Positive stress triaxiality χ

Figure 10 shows SEM observations of smooth tension specimens ($\chi \simeq 1/3$), see Figure 5 for the corresponding stress-strain curve. Voids are found near the fracture surface. They appear to nucleate mainly on interfaces between α and β phases, although a few very small cavities are found within primary α grains. This is consistent with the observations made by Helbert et al(1996). The loading rate does not seem to have any direct effect on void nucleation.

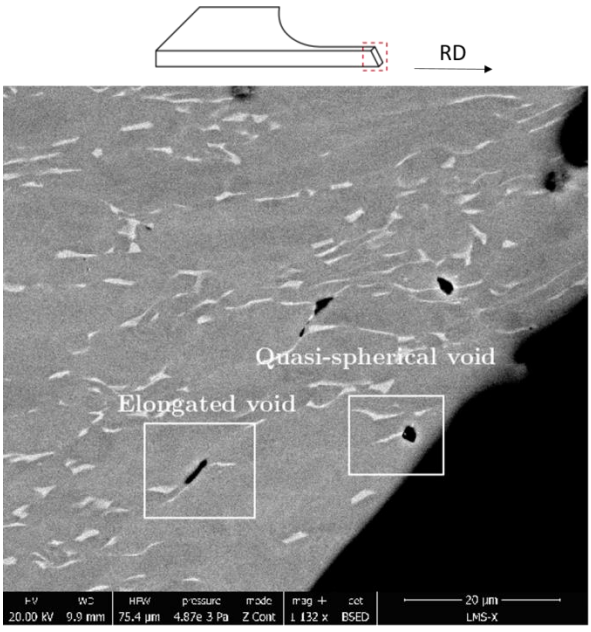

Figure 10: SEM observation of microvoids on a longitudinal section of a smooth tensile specimen fractured at $350s^{-1}$ along RD

The same type of observations was carried out on notched TD specimens ($\chi \simeq 1/2, 2/3, 1$). As in the smooth specimens, some cavities are found near the fracture surface (see Figure 11a for $\chi \simeq 1/2$) , see Figure 7 for the corresponding stress-strain curve. However, these cavities become scarcer away from the fracture surface, in spite of the considerably higher stress triaxiality ratio.

In an attempt to determine at which stage the cavities were formed, a test on a notched specimen was interrupted just before fracture (ε ≈3.3%) and a longitudinal section was observed (see

Figure 11b). Some cavities were found near the free surfaces, indicating that, although it remains limited, diffuse damage took place before fracture, under high stress triaxiality ratios.

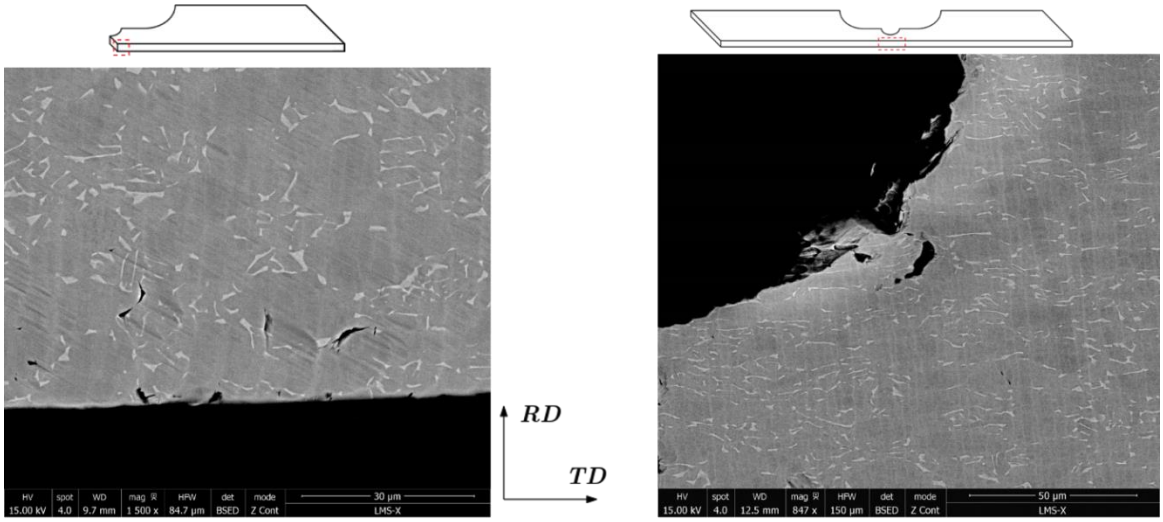

(a) Fractured $\varepsilon_f \simeq 3.8$

(b) Non broken $\varepsilon_f \simeq 3.3$ %,

Figure 11: SEM observations of longitudinal sections of notched tension TD specimens (R=2mm, $\chi \simeq 1/2$, $\dot{\varepsilon} = 10^{-3}s^{-1}$).

Figure 12 presents macroscopic views of the broken smooth tension specimens ($\chi \simeq 1/3$) loaded along RD, TD and DD directions at low strain rate, at room temperature. Both the front and side views are shown. For the three cases, the fracture surface is inclined into the thickness. According to the side view, for both the RD and TD specimens the fracture surface is rather smooth (a bifurcation is however visible for TD) and is inclined at 45º, while for the DD specimen the fracture surface has a parabolic shape with two branches inclined at about +/- 45º. Shear strain localization, thus does not seem to follow the rows of α nodules perpendicular to ND mentioned above.

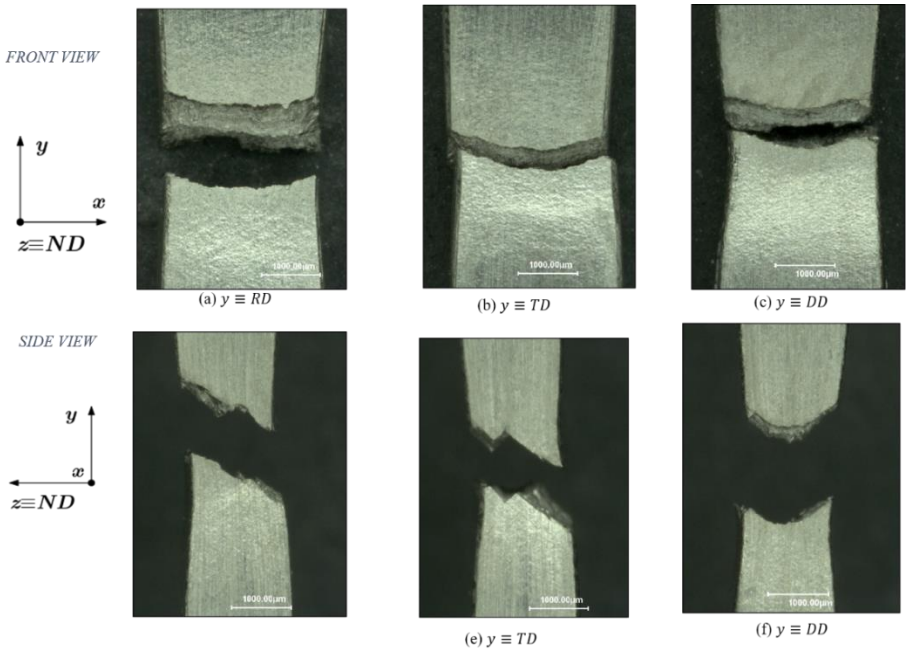

Figure 12: Broken smooth tensile specimens ($\chi \simeq 1/3$). $\dot{\varepsilon} = 10^{-3}\mathrm{s}^{-1}$

Figure 13 shows the fracture surface of a notched TD specimen (notch radius 2mm, $\chi \simeq 1/2$). The surface is very rough showing heterogeneities of all sizes. A closer look reveals extremely dense clusters of more or less equiaxed dimples. These features suggest the nucleation, growth, and coalescence of voids favoured by a high hydrostatic tension. Furthermore, although no obvious signs of the fracture initiation site are found, it is speculated to be close to the center (expected maximum stress triaxiality) considering the large, uneven features around the middle, and the absence of directional features near the edges.

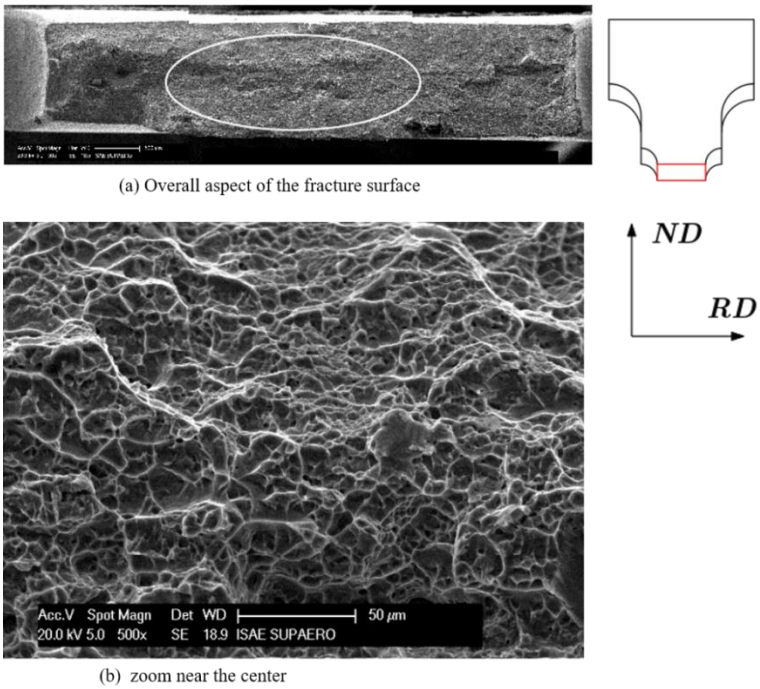

Figure 13: a) SEM micrograph of a notched TD specimen (R= 2 mm, $\chi \simeq 1/2$). $e_f \simeq 3.8$ %, 10^{-}

$^{3}s^{-1}$. White ellipse: likely place of crack initiation, b) Zoom near the center

A similar observation was performed for the notched tension specimen of radius 0.5mm notch radius, $\chi \simeq 2/3$, (see Figure 14). For this TD sample, the aspect of the surface seems comparatively more uniform than for the larger notch radius. The same type of equiaxed dimples is retrieved. In this case, fracture seems to have initiated from the notch roots, where the surface roughness is significantly larger. The reason behind this might be a larger plastic strain in this area, combined with a sufficiently high stress triaxiality ratio. The maximum χ is speculated to occur away from the center-line. This hypothesis will be confirmed by numerical simulations presented in the following Section.

Nil stress triaxiality χ

A substantial distribution of cavities, or even micro-cracks, was observed in a tension-induced shear TD specimen ($\chi \simeq 0$) after an interrupted test (see Figure 15). This was somewhat unexpected, considering the rise of the critical equivalent plastic strain for cavity nucleation in Titanium alloys reported at low hydrostatic pressure by Helbert et al (1996).

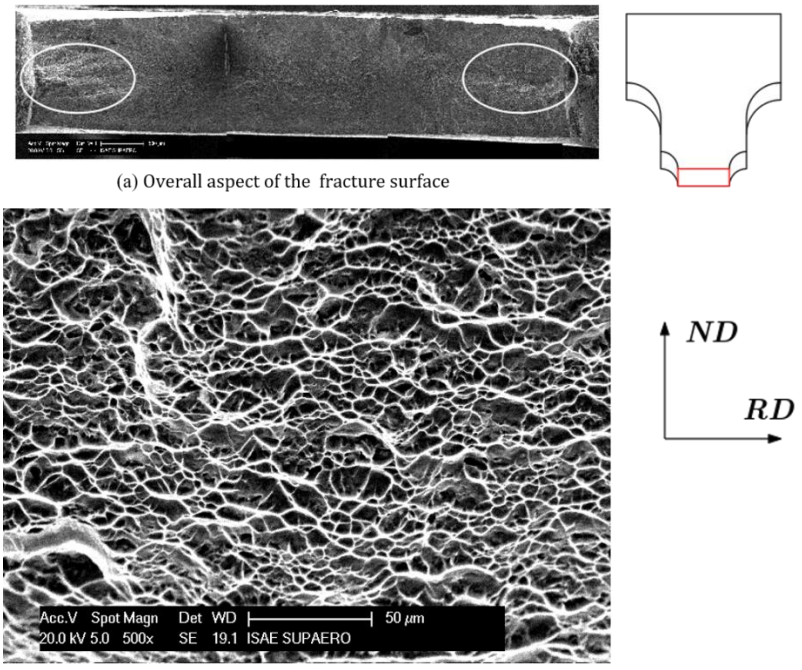

(a) Overall aspect of the fracture surface

(b) zoom near the notch root

Figure 14: SEM micrograph of a notched TD specimen (R=0.5mm, $\chi \simeq 2/3$). $\varepsilon_f \simeq 2.5$ %, $\dot{\varepsilon}=10^{-3}s^{-1}$. White ellipses: likely places of crack initiation. b) Zoom near the notch root

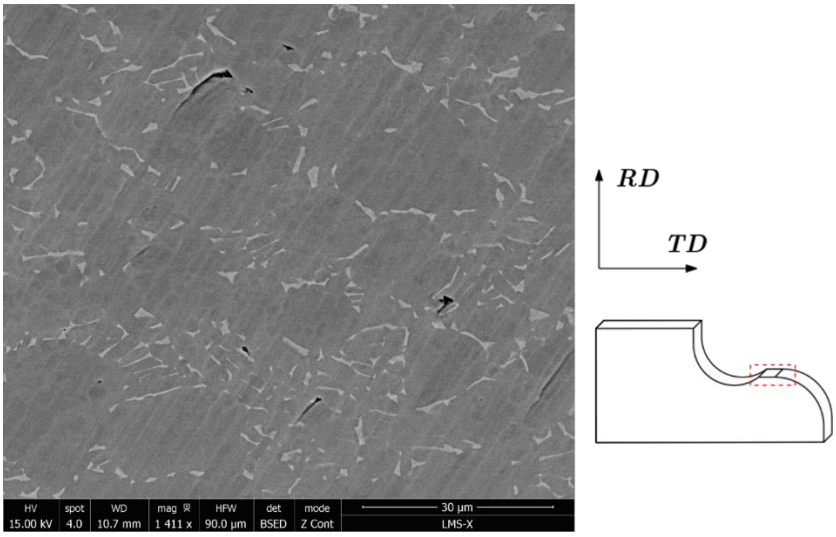

Figure 15: SEM observation of a longitudinal section of a shear TD specimen ($\chi \simeq 0$) after a test interrupted at $\varepsilon \simeq 9\%$, $\dot{\varepsilon}=10^{-3}s^{-1}$.

Figure 16 shows the smooth fracture surface of such a TD specimen, normal to the free surface and parallel to the tensile axis. It looks heterogeneous, and exhibits clusters of elongated dimples surrounded by smooth, mated zones.

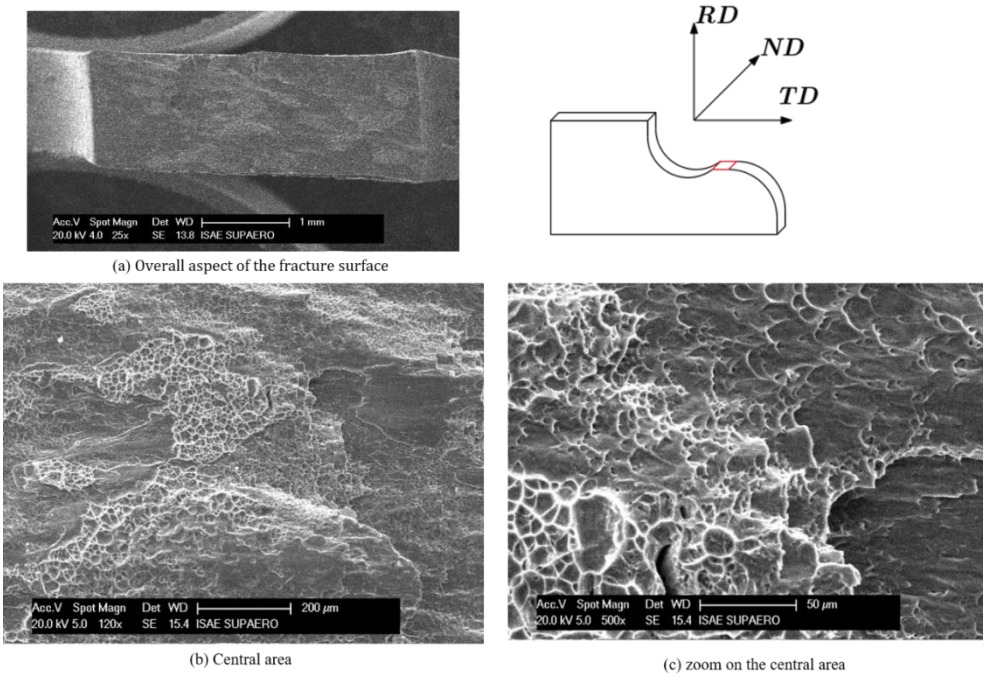

Figure 16: SEM observations of a broken shear TD specimen ($\chi \simeq 0$). $\varepsilon_f \simeq 9$ %, $10^{-3}s^{-1}$.

Negative stress triaxiality χ

The fracture of smooth compression specimens ($\chi \simeq -1/3$) is sudden, precocious and localized

in a band inclined by 45º with respect to the compression axis. Figure 17 shows a SEM observation of such a fracture surface, which exhibits mated areas surrounding elongated dimple clusters. These micrographs show a great resemblance with those presented in Lee and Lin(1997).

Compression tests on hat-shaped specimens for which macro crack propagation had begun were successfully stopped (see Figure 18 for $\chi \simeq -1/2$ at low and high strain rates). The macro cracks, initiated from all inner and outer corners, and propagated (quasi) symmetrically along a seemingly straight path joining the two corners. However, when zooming on the crack tip, a staircase-shaped trajectory appears, as the likely result of the coalescence of some diffuse micro-cracks nucleated under shear. Such a crack shape had been observed in other Ti-6Al-4V alloys loaded at high strain rate (see Longère and Dragon(2015), Dorothy and Longère (2019), and Peirs et al. (2010).

In the Meyers's geometry ($\chi \simeq -1/5$) deformed under shear loading, multiple cracks also nucleated from the corners of the specimen, and – as in the other hat-shaped geometry – seemed to grow as the result of the coalescence of micro-cracks generated along their path.

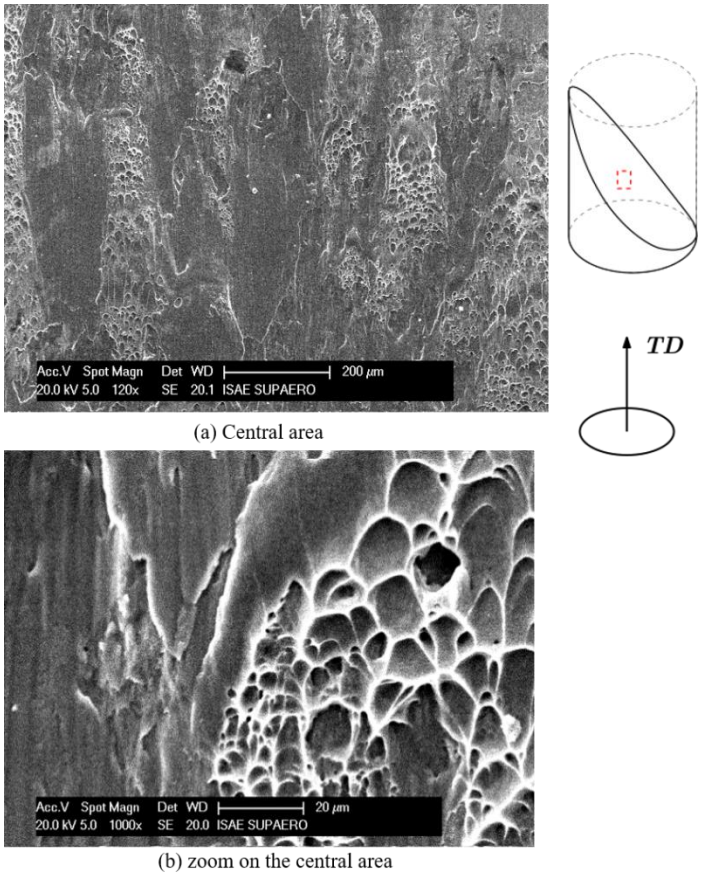

(a) Central area

(b) zoom on the central area

Figure 17: SEM observations of the fracture surface of a compression TD specimen ($\chi \simeq -1/3$). $\varepsilon_f \simeq 17$ %, $\dot{\varepsilon}=10^{-3}s^{-1}$.

2.4 Synthesis of the observations

Comparing all the above presented micrographs, one can distinguish two different fracture mechanisms described by many authors: (i) a shear-driven mechanism, under negative χ (compression and shear loadings), and (ii) a cavity nucleation/growth and coalescence mechanism, typical of positive χ. This competition between shear localization and micro-voiding must accordingly be accounted for in the formulation of a fracture criterion.

Damage, in the form of micro-cavities, nucleated mostly at α/β interfaces, was found near the fracture surfaces. The latter were often inclined by 45º into the thickness of smooth tension specimens. Depending on the loading conditions, shear-driven strain localization and damage, leading to slanted fracture with limited necking, or more diffuse, triaxiality-driven cavities nucleation, growth and coalescence leading to fracture with more substantial necking were observed. No clear conclusions can be drawn on the influence of strain rate, or even the loading direction.

A significant ductility is evidenced, with only a weak micro-voiding induced damage activity before failure. One can thus conclude that the coupling between micro-voiding induced damage and elasticity/plasticity only plays a minor role, and may accordingly be neglected. In other words, there seems to be no need for a coupled damage-plasticity model – see e.g. Longère et al. (2012), Longère and Dragon (2016) and Hfaiedh et al. (2018) for situations wherein damage-plasticity coupling is needed.

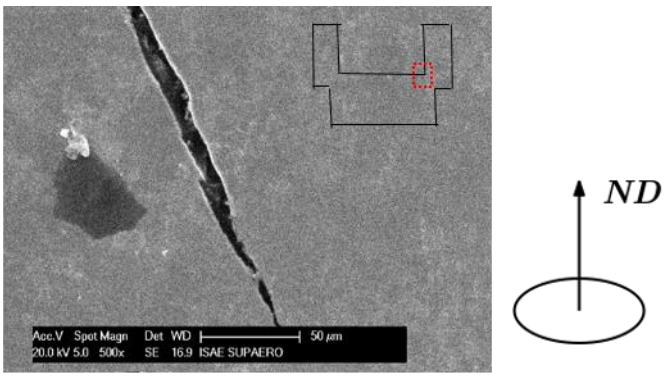

(a) $\dot{u} = 0.5\text{mm/min}$

(b) $\dot{u} = 5\text{x}10^{3}\text{mm/s}$

Figure 18: Couque's hat-shaped ND specimens ($\chi \simeq -1/2$) after partial fracture. (a) $\dot{u} =$

0.5mm/min , and (b) $\dot{u} = 5\text{x}10^{3}\text{mm/s}$

3 Numerical analyzes

The constitutive model used to simulate the tests, detailed in Ruiz de Sotto et al. (2020-a) and outlined in Appendix, does not account for damage, but captures the anisotropic behavior, rate dependence, tension-compression asymmetry and isotropic/kinematic hardening of the material. It has been implemented as a user material subroutine in the explicit version of the commercial finite element code LS-DYNA LSTC (2018) and used for three-dimensional numerical simulations of the experimental configurations (using the mass scaling option for quasi-static tests), in order to estimate the local evolutions of the plastic strain κ (see Appendix for the definition), stress triaxiality ratio χ and Lode parameter L in the critical area, unreachable by the experiment.

Selectively reduced (S/R) integration 8-node solid element (8 integration points with constant pressure throughout the element), also known as "elform 2" or bricks in LS-DYNA, are used. In order to check the mesh objectivity of the numerical results, various mesh sizes are considered.

While all loading cases reported in Section 2 have been numerically simulated, only four examples are detailed below for sake of brevity: (i) tension on flat smooth specimens, (ii) tension on flat notched specimen, and (iii) tension-induced shear loading on flat half-smiley specimen, and (iv) compression-shear on hat-shaped specimens.

Figure 19 shows the specimens' sketches with the boundary conditions. Accounting for through-thickness, through-width and through-length symmetries of the flat, smooth and notched, tension specimens, only one eighth of the specimens is modelled with adequate boundary conditions. Accounting for through-thickness symmetry of the half-smiley specimen, only half of the specimen is meshed with adequate boundary conditions. Hat-shaped specimens exhibit a symmetry of revolution, but due to the plastic anisotropy of the material, axisymmetric simulations would not be correct. A quarter of the Couque and Meyer specimen are thus meshed with adequate boundary conditions. The controlled displacement (at constant velocity) is applied to the nodes of the top side while the bottom side is constrained in the vertical direction.

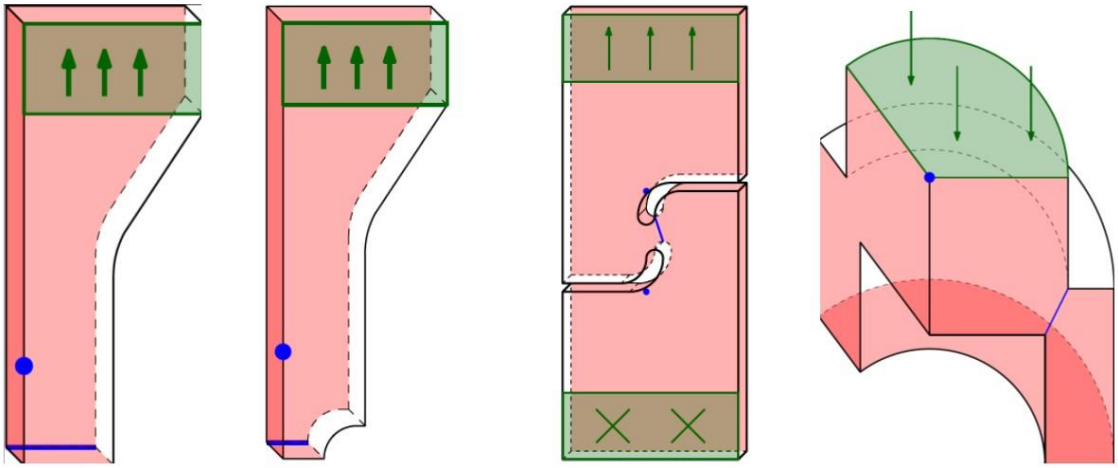

Figure 19: Geometries and boundary conditions for the numerical simulations. The green areas represent the imposed displacement (or fixture) and the red zones the symmetry conditions. The parts where internal variables are extracted are indicated by blue lines.

3.1 Uniaxial tension

The smooth tension specimens were modelled with three mesh sizes of 50, 100 and 200 μm in the gauge length. The axial plastic strain field in the three deformed meshes are compared in Figure 20a at an advanced stage of deformation involving necking. The specimen grip part with larger mesh sizes is not represented. In Figure 20b the experimental dimensionless force-displacement curve for tension along RD at low strain rate is compared with the curves obtained considering the three mesh sizes. It can be seen that the experimental curve is well captured, and that there is no significant mesh dependence. This comment also applies to the other loading directions, see Ruiz de Sotto et al. (2020).

Numerical simulations at high loading rate were conducted for mesh sizes of 50 and 100 μm in the gauge length. Figure 20d shows a comparison between the numerical and the experimental results. Independently of the mesh size, the numerical curve is oscillatory. This simulation artefact is due to the mechanical waves induced by the rapid loading that keep bouncing between the boundaries. This undesirable effect may be fixed by modelling the whole specimen and the input and output bars, so that the wave can be reflected/transferred from/outside the specimen. The smoothing of such oscillations by averaging every three consecutive points yields a curve close to the experimental one, with no significant mesh dependence.

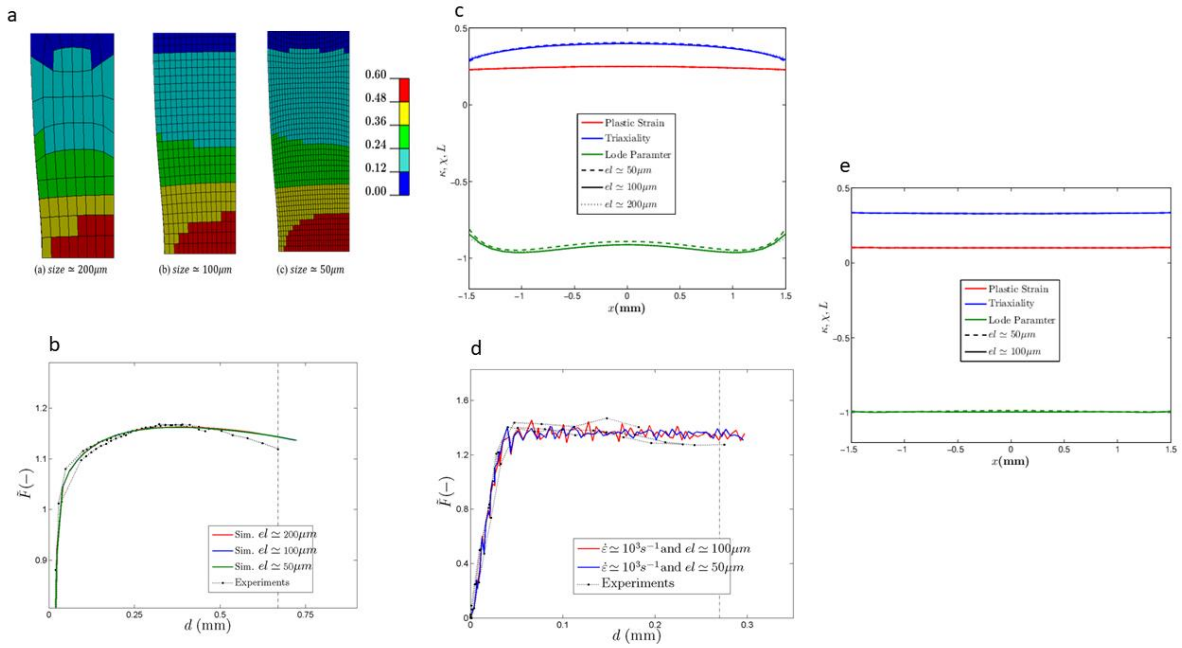

Figure 20: Simulation of the tensile tests along TD on smooth specimens, using three different mesh sizes. a) comparison of the plastic strain fields at $10^{-3}s^{-1}$, b) normalized load-displacement curves at $10^{-3}s^{-1}$, c) transverse profiles of plastic strain κ, stress triaxiality χ and Lode parameter L at mid-length at $10^{-3}s^{-1}$, the point where fracture is expected to initiate is indicated by a vertical line, d) normalized load-displacement curves at $10^{3}s^{-1}$, e) transverse profiles of plastic strain, Lode parameter and triaxiality at mid-length at $10^{3}s^{-1}$

In addition, the plastic strain κ, stress triaxiality χ and the Lode parameter L profiles computed along the horizontal symmetry line of the specimen, at mid thickness converge for a mesh size of 100 μm (see Figures 20d and e).

3.2. Tension on notched specimens

Figure 21 compares the experimental dimensionless load-displacement curves to the ones obtained from simulations run with two different mesh sizes of 50 and 100 μm, for the notches of $R = 2\text{mm}$ ($\chi \simeq 1/2$) and $R = 0.5\text{mm}$ ($\chi \simeq 2/3$). Within the displacement range covered by the experimental curves, no effect of the element size is observed on the global scale.

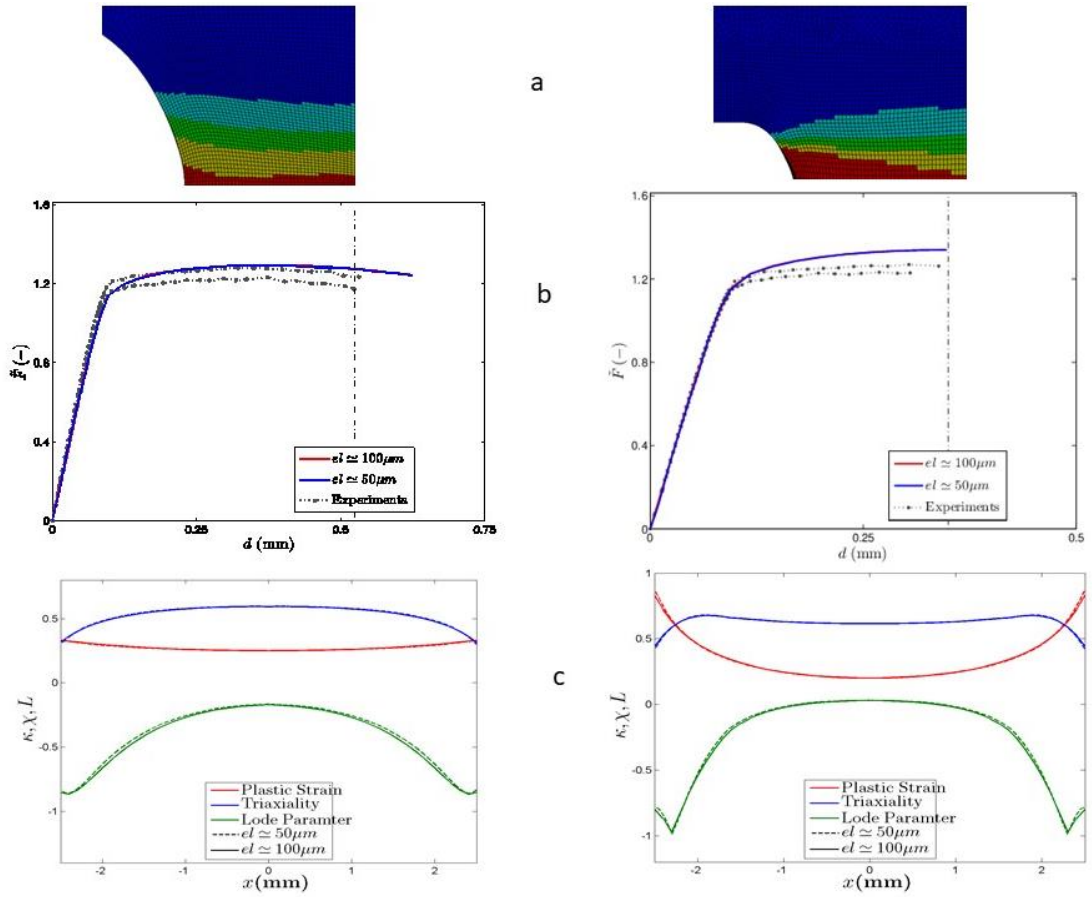

Figure 21: Simulation of the tensile tests along RD on simply notched specimens, using two mesh sizes for R=2mm (left) and R=0.5mm (right) a) Plastic strain fields computed with the fine mesh, b) normalized load-displacement curves, c) transverse profiles of plastic strain κ, stress triaxiality χ and Lode parameter L at mid-length at the instant when fracture is expected to initiate, indicated by a vertical line on Figure 21b

In Figure 21b, the plastic strain and the stress triaxiality ratio profiles along the width of simply notched specimens are plotted from one notch root to the other at the instant when fracture is expected to initiate, indicated by a vertical line on Figure 21b. Concerning the wider notch ($R = 2$mm and lower stress triaxiality χ), the maximum values of stress triaxiality are found at mid-width, and the stress triaxiality χ quickly decreases towards the notch roots. As for the plastic strain, it is relatively uniform irrespective of the lateral position (especially at large strain).
A different trend is seen for the sharper notch ($R = 0.5$ mm and higher χ). The stress triaxiality remains quasi-constant over most of the width (the maximum values are found close to the edges), whereas the plastic strain is substantially higher near the notch roots, where it is up to three times larger than at the center.

3.3 Tension-induced shear loading

The effect of the mesh size for the tension-induced shear specimen is shown in Figure 22 in terms of strain field, computed dimensionless load-displacement curves, and profiles of the plastic strain, Lode parameter and triaxiality along a vertical line joining two notch roots.

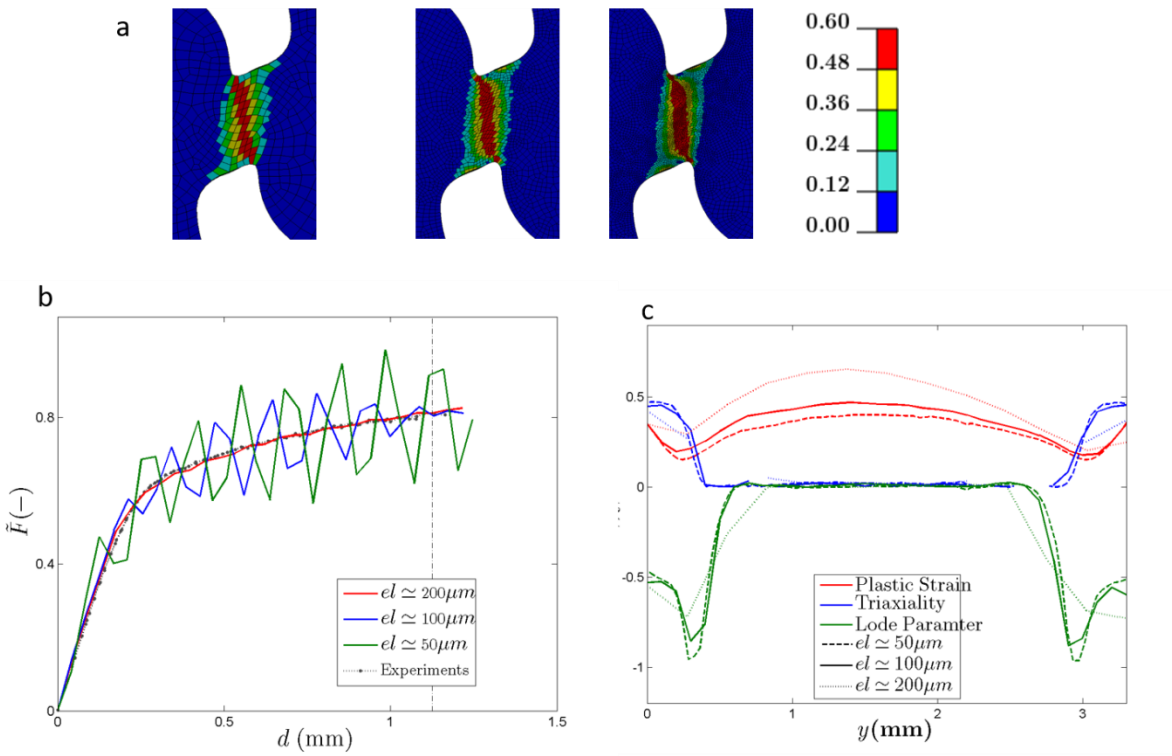

Figure 22: Simulation of the tensile tests along RD on shear specimens, at 1.6^{-3}mms^{-1}, using three mesh sizes a) Comparison of the plastic strain fields, b) normalized load-displacement curves, c) profiles of plastic strain κ, stress triaxiality χ and Lode parameter L along a vertical line joining two notch roots. The instant when fracture is expected to initiate is indicated by a vertical line in Figure 22b

As visible in Figure 22b, as the mesh is refined in the sheared area, an oscillatory behaviour appears, similar to the one observed in the simulation of dynamic tension on the smooth specimen, in Figure20d. The reason might be the mesh heterogeneity between the sheared area (fine mesh) and the surrounding part (coarser mesh) producing undesired stress discontinuities. Though the oscillatory response is visible on the overall reaction force at the head of the specimen, the plastic strain κ, the stress triaxiality ratio χ and the Lode parameter L do not present such behaviour, as observed on the profiles computed along the vertical line joining the two notch roots in Figure 22c. The predicted values are only slightly dependent on the element size, except maybe for the plastic strain, for which a too rough mesh produces larger errors. It is assumed that an element size of 100 μm is enough for a converged solution.

Moreover, although plastic strain eventually develops at the notch roots, the largest strain remains localized near the centre of the sheared area. Therefore, assuming a good correlation with the experimental strain fields, it is expected that damage and fracture would initiate near the centre.

3.4. Compression-shear loading

Figure 23a compares the measured and simulated normalized load-displacement curves for the hat-shaped specimens loaded along ND. For the latter, two extreme boundary conditions were considered: either frictionless contact between the sample and the holding device, which seems reasonable, since some lubricant was used, or fully constrained sliding displacement on the outer surface. For Meyer's samples (STR ≈-0.2), the choice of one or the other boundary condition has a negligible effect, and a reasonable agreement between simulations and tests can be observed. Figure 23b shows the profiles of the plastic strain κ, stress triaxiality χ and the Lode parameter L along the blue line plotted in Figure 19c. For Couque's samples ($\chi \approx$ -0.5), the effect of free or constrained sliding is slightly more pronounced, but the measured response is not accurately captured, whatever the boundary condition. The proposed constitutive model needs to be improved to reproduce the response of the material under such negative stress triaxiality.

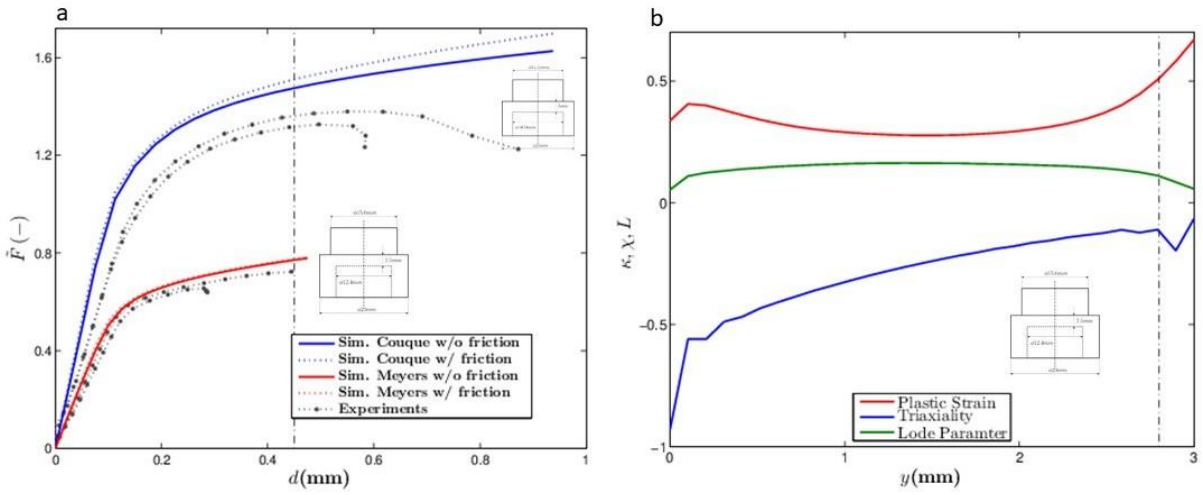

Figure 23: a) Measured and simulated normalized load-displacement curves for hat-shaped compression-shear specimens, v = $8x10^{-3}$ mms^{-1}, loaded along ND, b) profiles of plastic strain κ, stress triaxiality χ and Lode parameter L profiles along the blue line plotted in Figure 19c, at the instant when fracture is expected to initiate, indicated by a vertical line in Figure 23a

3.5 Fracture loci

The local loading paths leading to fracture may be described through the evolutions of the stress triaxiality ratio χ and Lode parameter L that the different specimens have undergone at their most critical point along plastic deformation. It provides an insight on how damage and subsequent fracture occur as a function of the stress state.

Figure 24 shows the different loading paths computed with finite elements of the S/R type with a size of approximately 100 µm. The element whose loading path has been plotted is the innermost element in the cross-section of the considered specimens, i.e. the furthest point from the notches or edges. This choice is based on the assumption that the highest χ is found away from any free surface. However, for the notched geometry of radius $R = 0.5$mm, the loading path were computed at an element close to the notches (as justified by the microscopic

observations and corroborated below).

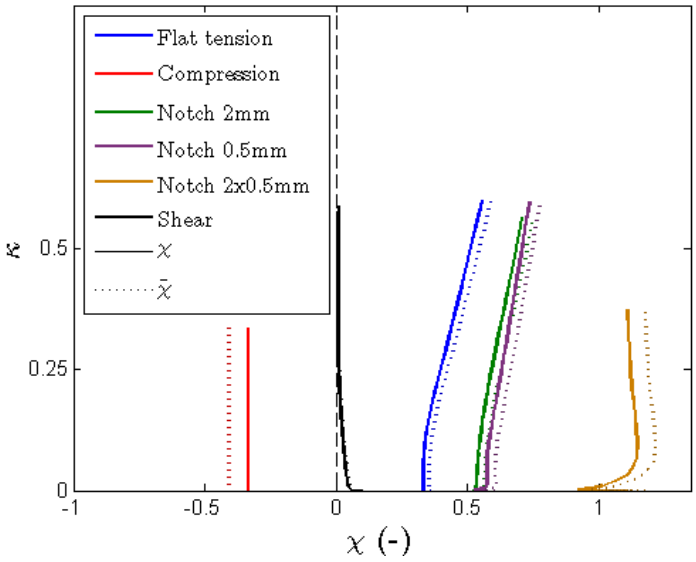

Figure 24: Loading paths at the critical point for the different geometries in terms of plastic strain κ as a function of the stress triaxiality ratio χ. $\dot{\varepsilon} \simeq 10^{-3} s^{-1}$, loading along TD. The two definitions for the stress stress triaxiality ratios involve either Von Mises stress or the equivalent stress issued from the constitutive model described in appendix

Depending on the definition used for the stress triaxiality ratio (using Von Mises stress, or an equivalent stress related to the anisotropic constitutive model, equation 9 in the appendix) as explained in the introduction, the loading paths may appreciably change. For instance, $\tilde{\chi}$ in compression is slightly more negative than χ ($\tilde{\chi} < \chi \simeq -1/3$). Conversely, the tension specimens present higher values of $\tilde{\chi}$. However, no large discrepancies are seen for the shear conditions. Based on a comparison with values available in literature, the first definition of χ based on Von Mises stress is retained in the sequel.

According to Figure 24, the stress triaxialities χ are comparatively more positive in the notched specimens than for the smooth samples, as expected. Both simple notches of $R = 2\text{mm}$ ($\chi \simeq 1/2$) and $R = 0.5\text{mm}$ ($\chi \simeq 2/3$) yield relatively close results. On the other hand, the doubly notched specimen reaches a much higher positive triaxiality ratio ($\chi > 1$). Surprisingly enough, after some initial plastic deformation, the stress triaxialitiy reaches a steady value close to 1.2. Finally, the tension-induced shear specimen ($\chi \simeq 0$) deforms under nearly pure shear stress ($\chi = 0$).

Figure 25 displays an estimation of the plastic strain value at which the different specimens fail (represented by a dot) superimposed on the loading path. In order to find these values, the global strain at fracture measured with the extensometer is compared with the one obtained from the virtual extensometer in the simulation. The global strain at which the specimen is supposed to fail is used to extract the local plastic strain in the finite element of interest. Table 4 gathers the final values of κ, χ and L for all the successfully simulated types of tests, considering the latest fracture among duplicated tests.

Table 4: Local plastic strain at fracture, stress triaxiality and Lode parameter at fracture computed at the critical point. The values for Couque's specimen are approximate (see above)

	Specimen type	Fracture strain, κ	Stress triaxiality, χ	Lode parameter, L
RD	Smooth compression 10^{-3} s^{-1}	0.25	-0.33	1
	Shear	0.36	0.01	0
	Smooth tension 10^{-3} s^{-1}	0.2	0.38	-0.94
	Smooth tension 300 s^{-1}	0.14	0.33	-0.99
	Notched 2 mm	0.25	0.6	-0.15
	Notched 0.5 mm	0.2	0.62	-0.26
	Doubly notched	0.1	1.17	-0.07
TD	Smooth compression 10^{-3} s^{-1}	0.16	-0.33	1
	Shear	0.39	0.01	0.01
	Smooth tension $10^{-3}s^{-1}$	0.25	0.4	-0.9
	Smooth tension 300 s^{-1}	0.13	0.33	-0.99
	Notched 2 mm	0.26	0.6	-0.16
	Notched 0.5 mm	0.2	0.61	0.27
	Doubly notched	0.1	1.15	-0.07
DD	Smooth compression 10^{-3} s^{-1}	0.28	-0.33	1
	Shear	0.44	0.03	0
	Smooth tension 10^{-3} s^{-1}	0.44	0.49	-0.8
	Smooth tension 300 s^{-1}	0.18	0.34	-0.98
	Notched 2 mm	0.27	0.6	-0.1
	Notched 0.5 mm	0.27	0.67	-0.22
	Doubly notched	0.12	1.15	0
ND	Couque 10^{-3} s^{-1} (approximations)	≈ 0.4	$\approx$ -0.75	≈ 0.1
	Meyer 10^{-3} s^{-1}	0.67	-0.43	0.1
	Smooth compression 10^{-3} s^{-1}	0.38	-0.33	1
	Smooth tension $10^{-3}s^{-1}$	0.15	0.36	-0.93

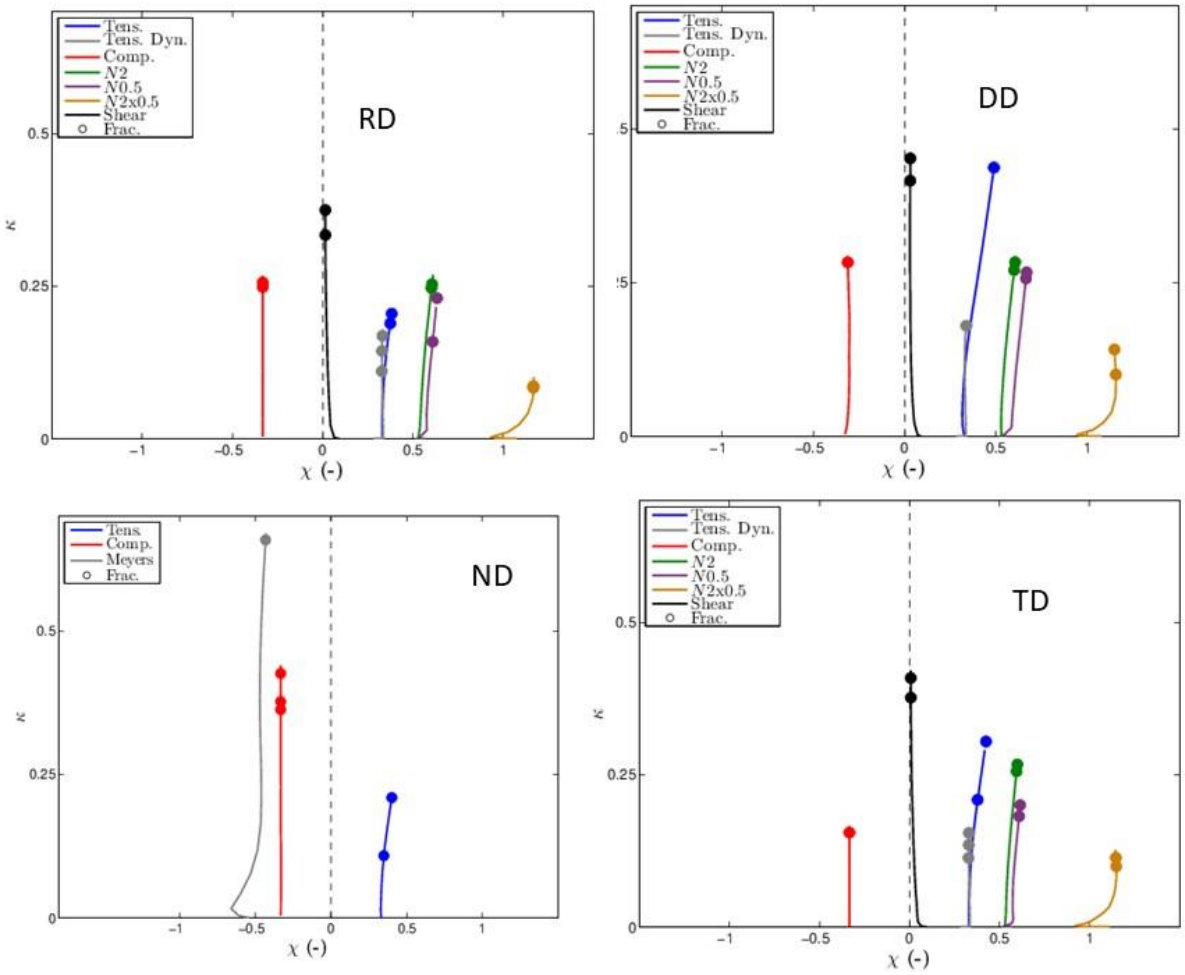

Figure 25: Plastic strain κ vs. stress triaxiality ratio χ for all loading directions. The dots indicate fracture.

Figure 25 suggests a smaller strain to fracture when the triaxiality increases in absolute values, with a maximum ductility for χ close to zero, except along ND where the peak ductility seems to be shifted towards a negative triaxiality. This result is appreciably different from the fracture locus obtained for AA2024 by Bao and Wierzbicki(2004) . This result is however consistent with the evolution found by Papasidero et al. (2015) for the same aluminium alloy, and with the conclusion of a ductility higher in shear than in tension drawn by Gross et al. (2016) as well as by Wang et al. (2019) for Ti-6Al-4V. Regarding the strictly positive stress triaxiality range, the strain to fracture decreases as the stress triaxiality χ becomes more positive. This expected result is in accordance with Rice and Tracey's (1969) and Johnson-Cook's (1985) fracture loci. The lower ductility found here for a small negative triaxiality, as compared to pure shear – at least for loadings along RD, TD and DD – seems actually in agreement with the results of Vilotic et al. for Ti-6Al-4V(2016) , since their Figure 6 shows a fracture strain for χ close to -0.4, lower than for $\chi = 0$, and then a rise in ductility, as the triaxiality gets more negative. Additional tests in such conditions would be useful to confirm and explain this tendency.

The evolution of the local plastic strain κ as a function of the local Lode parameter L at the same elements as in Figure 25 is plotted in Figure 26. No clear trend emerges from the latter,

except a peak of ductility for a Lode parameter close to 0.

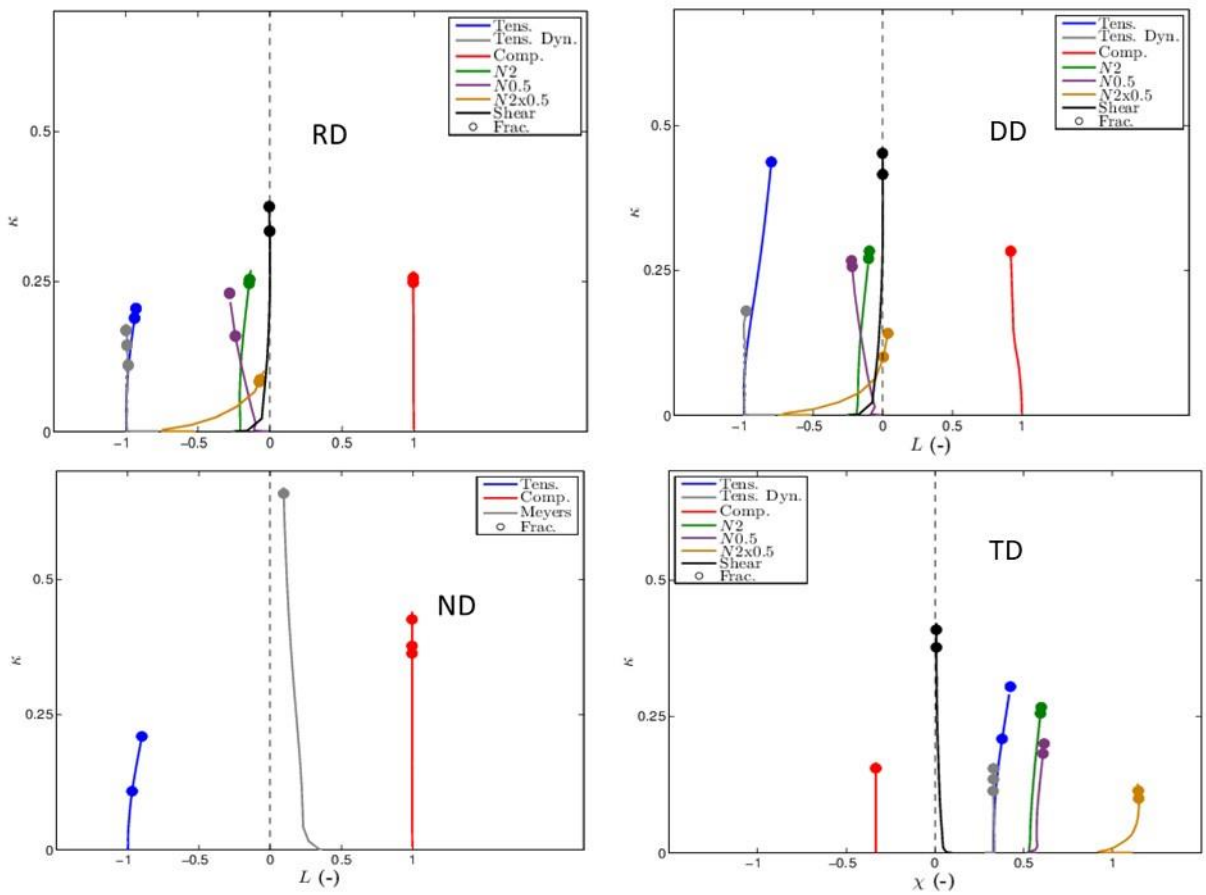

Figure 26: Plastic strain κ vs. Lode parameter, *L* for all loading directions. The dots indicate fracture.

4 Concluding remarks

A series of mechanical tests have been carried out in the stress triaxiality range [-1/2,1] and for strain rates ranging from 10^{-3} to 1500 s^{-1} on a Ti-6Al-4V titanium alloy along various loading directions. Microscopic observations of broken specimens have been achieved in order to document the underlying damage mechanisms. While the growth and coalescence of cavities (nucleated mostly at α/β interfaces) control ductile fracture at positive triaxialities, strain localization, and shear mode cracking dominate at zero and negative triaxialities.

Given the limited micro-damage and the rather brutal drop in stress at failure, a fracture criterion considering a damage indicator seems to be suitable for the Ti-6Al-4V titanium alloy under consideration. Yet, another batch (with e.g. a different heat treatment) may potentially fail differently and possibly require the use of a coupled damage-plasticity model, see Longère and Dragon (2015).

In the present case, the plastic strain at failure is weakly dependent on the strain rate in the considered range, and may be expressed in a first approximation via an exponentially

decreasing function of the absolute value of the stress triaxiality ratio. This function depends significantly on the loading direction, with nearly a factor of two between the most and least ductile directions. These directions change between tension and compression, probably because of changes in the contribution of mechanical twinning. This tension-compression asymmetry in terms of anisotropy in ductility makes the formulation of an anisotropic fracture criterion difficult.

By contrast, no clear dependence on the Lode parameter or strain rate was found.
Accordingly, the fracture criterion proposed by Bao and Wierzbicki (2004) and Wierzbicki et al. (2005) must not be considered as universal, and there actually exists no universal cut-off value for negative stress triaxiality, viz. -1/3. Indeed, this cut-off value was derived from a series of tests carried out on a very specific class of materials (AA2024-T351 aluminum alloys) and is not physically supported for others. On the contrary, there are many experimental evidences in literature of failure occurring under STR lower than -1/3, (see e.g. Longère and Dragon (2015) or Vilotic et al. (2016)), so that shear decohesion is not bounded in the negative stress triaxiality range by a value of -1/3. In addition, an overall nil (and even negative) stress triaxiality at the macroscale does not necessarily imply that the stress triaxiality is nil or negative everywhere at the micro-scale, as shown in Longère and Dragon (2015), which explains the co-existence of smooth, sheared areas and dimple clusters in specimens after shear-compression loading until fracture.

The readers interested in attenuating the mesh dependence of the numerical results in presence of damage-induced softening can refer to Abu Al-Rub and Voyiadjis (2006), Voyiadjis and Abu Al-Rub (2006), and Allix (2012).

Appendix: Anisotropic viscoplastic Constitutive model

The viscoplastic, anisotropic constitutive model specifically formulated and identified for this batch of Ti-6Al-4V titanium alloy is detailed inRuiz de Sotto et al. (2020-a) . It accounts for plastic orthotropy, isotropic and kinematic hardening, tension-compression strength differential and viscosity, and is only briefly introduced in the following.

In the constitutive model, the set of state variables $\wp$ and conjugate state variables $\wp^c$ are:

$$\wp = \left(T, \underline{\underline{\varepsilon}}^e, \kappa, \underline{\underline{a}}\right) \Leftrightarrow \wp^c = \left(s, \underline{\underline{\sigma}}, r, \underline{\underline{X}}\right) \tag{5}$$

where $\left(T, \underline{\underline{\varepsilon}}^e, \kappa, \underline{\underline{a}}\right)$ represents temperature, elastic strain 2nd order tensor, isotropic hardening variable (and cumulated plastic strain) and kinematic hardening variable 2nd order tensor, and $\left(s, \underline{\underline{\sigma}}, r, \underline{\underline{X}}\right)$ entropy, Cauchy stress 2nd order tensor, isotropic hardening force and kinematic hardening force 2nd order tensor.

742 The rate form of the constitutive state laws in the corotational frame reads:

743

744 $$\dot{\underline{\underline{\sigma}}} = \underline{\underline{\underline{\underline{C}}}} : \dot{\underline{\underline{\varepsilon}}}^{e} - \alpha K \dot{T} \underline{\underline{\delta}} \; ; \; \dot{\underline{\underline{X}}} = \frac{2}{3} C \dot{\underline{\underline{a}}} \; ; \; \dot{r} = h''(\kappa) g(T) \dot{\kappa} + h'(\kappa) g'(T) \dot{T} \tag{6}$$

745

746 where (α, K, C) represent the thermal dilatation coefficient, bulk modulus and kinematic
747 hardening related constant. The stiffness 4th order tensor $\underline{\underline{\underline{\underline{C}}}}$, stored energy of cold work $h(\kappa)$
748 , and thermal softening function $g(T)$ are expressed as:

749

750 $$\begin{cases} \underline{\underline{\underline{\underline{C}}}} = \lambda \underline{\underline{\delta}} \otimes \underline{\underline{\delta}} + 2\mu \underline{\underline{\underline{\underline{I}}}} \\ h(\kappa) = \dfrac{Q_0}{n+1} \left(\varepsilon_0 + \kappa\right)^{n+1} - \dfrac{C}{D} \left[D\kappa - \exp\left(-D\kappa\right) \right] \\ g(T) = 1 - \left\langle \dfrac{T - T_{ref}}{T_m - T_{ref}} \right\rangle^{m_T} \end{cases} \tag{7}$$

751

752 where (λ, μ) are Lamé elasticity constants and $(Q_0, n, \varepsilon_0, D)$ isotropic hardening related
753 constants.
754 The yield function $f\left(\hat{\underline{\underline{\Sigma}}}, r; k\right)$ and plastic potential $F\left(\hat{\underline{\underline{\Sigma}}}, r; k\right)$ accounting for rate dependent,
755 non-associated plasticity read:

756

757 $$\begin{cases} f\left(\hat{\underline{\underline{\Sigma}}}, r; k\right) = \sigma_{eq}\left(\hat{\Sigma}_p; k\right) - \left[R_0 g(T) + r(\kappa, T) \right] = \sigma_v(\dot{\kappa}) \geq 0 \\ F\left(\hat{\underline{\underline{\Sigma}}}, r; k\right) = f\left(\hat{\underline{\underline{\Sigma}}}, r; k\right) + \dfrac{3D}{4C} \underline{\underline{X}} : \underline{\underline{X}} \end{cases} \tag{8}$$

758

759 where R_0 is a constant ($R_0 g(T_0)$ represents the initial size of the elasticity domain at
760 temperature T_0) and $\sigma_v(\dot{\kappa})$ the viscous stress. The transformed equivalent stress $\sigma_{eq}\left(\hat{\Sigma}_p; k\right)$ is
761 expressed as:

762

763 $$\begin{cases} \sigma_{eq}^{a}\left(\hat{\Sigma}_p; k\right) = \dfrac{1}{m_0^a} \displaystyle\sum_{p=1}^{3} \left(\left|\hat{\Sigma}_p\right| - k\hat{\Sigma}_p \right)^a \; ; \; \hat{\Sigma}_p = \mathrm{eig}_p\left(\hat{\underline{\underline{\Sigma}}}\right) \; ; \; \hat{\underline{\underline{\Sigma}}} = \underline{\underline{\underline{\underline{A}}}} : \left(\underline{\underline{s}} - \underline{\underline{X}}\right) \\ m_0^a = \left[\dfrac{2}{3}\left(1 - |k|\right) \right]^a + 2 \left[\dfrac{1}{3}\left(1 + |k|\right) \right]^a \end{cases} \tag{9}$$

764

765 where the constants (k, a) allow for describing the tension-compression asymmetry and shape

of the elasticity domain. $\mathrm{eig}_p\left(\hat{\underline{\underline{\Sigma}}}\right)$ is the p-th eigenvalue of $\hat{\underline{\underline{\Sigma}}}$. Voigt notation for $\underline{\underline{\underline{\underline{A}}}}$ yields the following 6x6 matrix representation

$$[A]=\begin{bmatrix} A_{11} & A_{12} & A_{13} & & & \\ A_{12} & A_{22} & A_{23} & & & \\ A_{13} & A_{23} & A_{33} & & & \\ & & & A_{44} & & \\ & & & & A_{55} & \\ & & & & & A_{66} \end{bmatrix} \tag{10}$$

where the A_{ij} terms are constants.

According to the normality rule, the evolution laws reads in the corotational frame:

$$\dot{\underline{\underline{\varepsilon}}}^p = \dot{\kappa}\underline{\underline{n}}\ ;\ \dot{\underline{\underline{a}}} = \dot{\underline{\underline{\varepsilon}}}^p - D\dot{\kappa}\underline{\underline{a}}\ ;\ \dot{T} = \frac{\beta\sigma_{vm}}{\rho c}\dot{\kappa} \tag{11}$$

where $\left(\dot{\underline{\underline{\varepsilon}}}^p, \underline{\underline{n}}\right)$ are the plastic strain rate and yield direction 2nd order tensors, and (β, ρ, c) the constitutive model consistent inelastic heat fraction (proportion of plastic work rate converted into heat), mass density and specific heat. One has also:

$$\begin{cases} \dot{\kappa} = \left\langle \dfrac{f}{Y_v} \right\rangle^{n_v}\ ;\ \sigma_v\left(\dot{\kappa}\right) = Y_v\dot{\kappa}^{1/n_v} \\ \underline{\underline{n}} = \dfrac{1}{m_0^a}\displaystyle\sum_{p=1}^{3}\left(\frac{\left|\hat{\Sigma}_p\right| - k\hat{\Sigma}_p}{\sigma_{eq}}\right)^{a-1}\left(\mathrm{sgn}\left(\hat{\Sigma}_p\right) - k\right)\underline{\underline{\underline{\underline{J}}}} : \underline{\underline{\underline{\underline{A}}}}\left(\underline{\nu}_p \otimes \underline{\nu}_p\right)\ ;\ \underline{\underline{\underline{\underline{J}}}} = \underline{\underline{\underline{\underline{I}}}} - \frac{1}{3}\underline{\underline{\delta}} \otimes \underline{\underline{\delta}} \\ \beta = \dfrac{\sigma_{eq} - r + \frac{2}{3}CD\underline{\underline{a}} : \underline{\underline{a}}}{\sigma_{vm}}\ ;\ \sigma_{vm} = \sqrt{\frac{3}{2}\underline{\underline{s}} : \underline{\underline{s}}} \end{cases} \tag{12}$$

For confidentiality reason, the values of the material constants are not provided.

5 Funding

The authors would like to acknowledge the financial support of the French Association Nationale Recherche Technologie (ANRT).

6 References

Abu Al-Rub R.K., Voyiadjis G.Z. (2006) A Finite Strain Plastic-damage Model for High Velocity Impact using Combined Viscosity and Gradient Localization Limiters: Part I – Theoretical Formulation. *Int. J. Dam. Mech.*, 15:293-334.

Allahverdizadeh N, Gilioli A and Manes A, Giglio M (2015) An experimental and numerical study for the damage characterization of a Ti-6Al-4V titanium alloy, *Int. Journ. Mech. Sciences* 93: 32-47.

Allix O. (2012), The bounded rate concept: A framework to deal with objective failure predictions in dynamic within a local constitutive model, *Int. J. Dam. Mech.*, 22-6:808-826

Bao Y and Wierzbicki T (2004) On fracture locus in the equivalent strain and stress triaxiality space, *Int Journ. Mech. Sciences* 46:81–98.

Bao Y and Wierzbicki T (2005) On the cut-off value of negative triaxiality for fracture, *Engng Fract. Mech.* 72: 1049–1069.

Barsoum I and Faleskog J (2007) Rupture mechanisms in combined tension and shear—experiments, *Int. J. Solids Struct.* 44 (6): 1768-1786

Chen G, Ren C, Lu L, et al. (2018) Determination of ductile damage behaviors of high strain rate compression deformation for Ti-6Al-4V alloy using experimental-numerical combined approach, *Engng. Fract. Mech.* 200: 499-520.

Coghe F, Tirry W, Rabet L, et al. (2012) Importance of twinning in static and dynamic compression of a Ti-6Al-4V titanium 835 alloy with an equiaxed microstructure, *Mater. Science Engng. A*537:1-10

Couque H (2003) A hydrodynamic hat specimen to investigate pressure and strain rate dependence on adiabatic shear band formation, *J. Phys. IV* 110: 423–428.

Dorothy H.L and Longère P (2019) Unified modelling of adiabatic shear banding and subsequent micro-voiding driven dynamic failure of viscoplastic solids, *Int. Journ. Impact Engng.* 132: 103322.

Dunand M, Gary G and Mohr D (2013) Load-Inversion Device for the High Strain Rate Tensile Testing of Sheet Materials with Hopkinson Pressure Bars, *Exper. Mech* 53: 1177–1188

Giglio M, Manes A and Vigano F (2012) Ductile fracture locus of Ti–6Al–4V titanium alloy, *Int Journ Mech. Sciences* 54:121-135.

Gross A and Ravi-Chandar K (2016) Prediction of ductile failure in Ti–6Al–4V using a local strain-to-failure criterion, *Int. Journ. Fracture* 98:221-245.

Ha J, Baral M and Korkolis YP (2019) Ductile fracture of an aluminum sheet under proportional loading, *Journ Mechanics Physics Solids* 132: 103685

Haltom SS, Kyriakides S and Ravi-Chandar K (2013) Ductile failure under combined shear and tension, *Int. J. Solids Struct* 50, 1507-1522.

Helbert AL, Feaugas X and Clavel M (1996) The Influence of Stress Triaxiality on the Damage Mechanisms in an Equiaxed α/β Ti-6Al-4V Alloy, *Met. Trans.* 27A :3043-3058

Hfaiedh N., Roos A., Badreddine H., Saanouni K. (2018), Interaction between ductile damage and texture evolution in finite polycrystalline elastoplasticity, *Int. J. Dam. Mech.*, 1-21

Hooputra H, Gese H, Dell H et al. (2004) A comprehensive failure model for crashworthiness simulation of aluminium extrusions, *Int. Journ. Crashworthiness* 9:449–464.

Huang J, Guo Y, Qin D et al. (2018) Influence of stress triaxiality on the failure behavior of Ti-6Al-4V alloy under a broad range of strain rates, *Theoretical & Applied Fract. Mech.* 97:48-61.

Jacques N, Mercier S and Molinari A (2012) Void coalescence in a porous solid under dynamic loading conditions; *Int J Fract* 173:203–213

Johnson G.R and Cook W.H (1985) Fracture characteristics of three metals subjected to various strains, strain rates, temperatures and pressures, *Engng. Fract. Mech.* 21-1: 31-48

Korkolis YP, Kyriakides S, Giagmouris T et al. (2010) Constitutive Modeling and Rupture Predictions of Al-6061-T6 Tubes Under Biaxial Loading Paths, *Journ Applied Mech*. 77: 064501-1- 064501-5

Lee WS and Lin MT (1997) The effects of strain rate and temperature on the compressive deformation behaviour of Ti-6Al-4V alloy, *Journ. Mater. Proc. Tech.* 71: 235–246.

Longère P and Dragon A (2015) Dynamic vs. quasi-static shear failure of high strength metallic alloys: Experimental issues, *Mech. Materials* 80: 203–218.

Longère P and Dragon A (2013) Description of shear failure in ductile metals via back stress concept linked to damage-microporosity softening, *Engng. Fract. Mech.* 98:92–108.

Longère P and Dragon A (2016) Enlarged finite strain modelling incorporating adiabatic shear banding and post-localization microvoiding as shear failure mechanisms. *Int. J. Dam. Mech.*, 25-8:1142-1169.

Longère P, Geffroy AG, Leblé B et al. (2012) Modeling the Transition between Dense Metal and Damaged (Microporous) Metal Viscoplasticity. *Int. J. Dam. Mech.*, 21:1020–1063.

LSTC (2018) LS-DYNA Theory Manual.

Meyers MA, Nesterenko VF, LaSalvia JC et al. (2001) Shear localization in dynamic deformation of materials: microstructural evolution and self-organization, *Mater. Science & Engng. A*317: 204–225

Pack K and Roth CC (2016) The second Sandia Fracture Challenge: blind prediction of dynamic shear localization and full fracture characterization, *Int. Journ. Fracture* 198:197-220.

Papasidero J, Doquet V, Mohr D (2015) Ductile fracture of aluminum 2024-T351 under proportional and non-proportional multi-axial loading: Bao–Wierzbicki results revisited, *Int. Journ. Solids & Struct* 69-70: 459-474.

Peirs J, Verleysen P, Degrieck J et al. (2010) The use of hat-shaped specimens to study the high strain rate shear behaviour of Ti–6Al–4V, *Int. Journ. Impact Engng.* 37:703–714.

Rice JR and Tracey DM (1969) On the ductile enlargement of voids in triaxial stress fields, *Journ. Mech. Physics Solids*17:201–217.

Roth CC and Mohr D (2018) Determining the strain to fracture for simple shear for a wide range of sheet metals, *Int. Journ. Mech. Sciences*149:224–240.

Roth CC, Gary G and Mohr D (2015) Compact SHPB System for Intermediate and High Strain Rate Plasticity and Fracture Testing of Sheet Metal, *Exper. Mech.* 55: 1803-1811.

Ruiz de Sotto M (2020-b), Characterization and modeling of the thermo-mechanical behavior of aTi-6Al-4V alloy under dynamic complex loading, PhD Thesis, Univ. Toulouse, France, https://hal.archives-ouvertes.fr/tel-03023834

Ruiz de Sotto M, Longère P, Doquet V and Papasidero J (2020-a) A constitutive model for a rate and temperature-dependent, plastically anisotropic titanium alloy, *Int. Journ. Plasticity 134*:102777.

Tancogne-Dejean T, Roth C.C, Woy U et al. (2016) Probabilistic fracture of Ti-6Al-4V made through additive layer manufacturing, *Int. Journ. Plasticity* 78:45–172.

Vilotic D, Movrin D and Alexandrov S (2016) A Ductile Fracture Criterion of Ti-6Al-4V at Room Temperature, *Exp. Mechanics 57*:59-366.

Voyiadjis GZ and Abu Al-Rub RK (2006) A Finite Strain Plastic-damage Model for High Velocity Impact using Combined Viscosity and Gradient Localization Limiters: Part II – Numerical Aspects and Simulations. *Int. J. Dam. Mech.*, 15:335-373.

Wang Q, Bruschi S, Ghiotti A et al. (2019) Modelling of fracture occurrence in Ti6Al4V sheets at elevated temperature accounting for anisotropic behaviour, *Int.Journ. Mech. Sciences* 150: 471-483.

Wierzbicki T, Bao Y, Lee YW et al. (2005) Calibration and evaluation of seven fracture models, I*nt. J. Mech. Sci*. 47, 719-743.

Zhang K, Badreddine H and Saanouni K (2018) Thermomechanical modeling of distortional hardening fully coupled with ductile damage under non-proportional loading paths, *Int. Journ. Solids & Struct.* 2144-145:123-136.

Zhang K, Badreddine H, Saanouni K (2020) Ductile fracture prediction using enhanced CDM model with Lode angle-dependency for titanium alloy Ti-6Al-4V at room temperature, *Journ. Mater. Proc. Tech.* 277: 116462.